Structural and Thermodynamic Characterization of Pt-$SrTiO_3$ Interfaces

Anna Altberg

Structural and Thermodynamic Characterization of Pt-$SrTiO_3$ Interfaces

Research Thesis

Submitted In Partial Fulfillment of the
Requirements for the Degree of Master of Science
In Materials Engineering

Anna Altberg

Submitted to the Senate of the
Technion – Israel Institute of Technology

Kislev, 5774 **Haifa** **November 2013**

Acknowledgements

I would like to express my gratitude to my supervisor, Prof. Wayne D. Kaplan for the guidance and help during this research.

I would also like to thank all my friends at the Technion, and especially my colleagues in the metal-ceramic interface group for their support and friendship.

I thank Dr. Y. Kaufmann, Dr. A. Berner and M. Kalina for their help and guidance.

I also wish to thank the Technion and an Irwin and Joan Jacobs Fellowship for their financial help.

Special thanks to my family and friends, and especially to my husband for all his support and patience.

Table of Contents

Acknowledgements 5

Table of Contents 7

List of Figures 10

List of Tables 14

Abstract 1

List of Symbols and Acronyms 3

1. Introduction 6

2. Literature Survey 8

2.1 Interfaces 8

2.1.1 Solid-Liquid Interfaces 8

2.1.2 Solid-Solid Interfaces 10

2.2 Solid State Dewetting 14

2.2.1 Terrace Ledge Kink (TLK) Model 16

2.3 Equilibrium Shape of Solids 19

2.3.1 Wulff Construction 20

2.3.2 Equilibrium Crystal Shape of a Solid Particle 21

2.4 Pt-$SrTiO_3$ System 23

2.4.1 $SrTiO_3$ 23

2.4.2 Pt-$SrTiO_3$ System 25

2.5 Research Goals 27

3. Experimental Methods 29

3.1 Sample Preparation 29

3.1.1 Substrate Preparation 29

3.1.2 Pt Film Deposition 29

3.1.3 Dewetting Experiments 30

3.1.4 Focused Ion Beam (FIB) 31

3.2 Characterization Methods 32

3.2.1 X-Ray Diffraction (XRD) 32

3.2.2 Scanning Electron Microscopy 33

3.2.3 Transmission Electron Microscopy 33

3.2.4 Scanning Tunneling Microscope (STM) 34

3.2.5 Simulations 34

4. Results 37

4.1 $SrTiO_3$ Morphology After BHF Treatment 37

4.2 Dewetting Results 38

4.3 Pt-$SrTiO_3$ Orientation Relationship 39

4.4 ECS of Pt 42

4.4.1 Determining the ECS 43

4.4.2 Chemical Analysis of Equilibrated Particles 44

4.5 Pt-$SrTiO_3$ Interfacial Energy 46

4.5.1 Particle-Substrate Misorientation 46

4.5.2 Determining the Interfacial Energy 47

4.6 Atomistic Structure of the Interface 48

4.6.1 HRTEM Analysis of the Interface 48

4.6.2 HAADF STEM Analysis 49

5. Discussion 52

5.1 ECS of Pt 52

5.1.1 Previous Works Conducted on ECS of Pt 52

5.1.2 Has the Particle Reached its ECS? 54

5.1.3 ECS of Supported Pt Particle Formed in High $P(O_2)$ 54

5.1.4 Chemical Analysis of Pt Equilibrated Particles 56

5.2 The Interfacial Energy between the Pt and $SrTiO_3$ 57

5.3 Substrate Morphology 58

5.4 Pt and (100)-$SrTiO_3$ Orientation Relationship 59

5.5 Experimental Limitations 61

6. Summary and Conclusions 63

7. Recommendations for Future Work 64

8. References 66

List of Figures

Figure 1: Schematic drawing of a liquid drop on a solid substrate. (a) The solid-liquid interface is flat and co-planar with the substrate (b) The solid-liquid interface is curved, forming a dihedral angle at the triple junction. 10

Figure 2: Illustration of the five macroscopic degrees of freedom of an arbitrary bicrystal interface. (a) The orientations of n_1, n_2 and n_r in a fixed coordinate system. (b) a tilt rotation of the two crystal coordinates systems so that n_1 is parallel to n_2, and (c) introduction of the twist component by rotating the top crystal n by the angle θ [7]. 11

Figure 3: (a) Schematic drawing of the side view of a bulk phase with a reconstructed surface. The reconstruction at the top layer affects a few layers beneath it. (b) and (c) Schematic drawing of a top view of reconstructed and unreconstructed bulk accordingly. 13

Figure 4: Phase contrast micrograph of the Ni–sapphire interface, showing periodic buckling of the of the terminating Ni layer (i.e. interface reconstruction) [14]..... 14

Figure 5: Model of a crystal surface showing monatomic height steps, kinks, single adatoms and terrace vacancies. Redrawn after Bonzel et al. [21] 17

Figure 6: Schematic energy diagram of different atomic sites of a simple cubic crystal 18

Figure 7: Schematic illustration of the Wulff construction, connecting the anisotropic surface free energy γ(θ), outer curve, with the equilibrium crystal shape function, inner curve (blue area). 21

Figure 8: Schematic drawing of the Winterbottom analysis for particles equilibrated on a substrate with different effective contact angles; (a) $\theta < 90^0$ and (b) $\theta > 90^0$..... 22

Figure 9: (a) $SrTiO_3$ cubic unit cell. (b) A 3D view of $SrTiO_3$ structure from <001> direction, showing alternative atomic layers of the TiO_2 and SrO in the cubic structure. 25

Figure 10: Schematic drawing of EBG evaporation system 30

Figure 11: Schematic drawing of experimental setup of dewetting experiments 31

Figure 12: SEM micrographs showing different stages of TEM sample preparation by FIB. (a) A plan-view of selected particle supported on the substrate. (b) This micrograph shows the process of milling a lamella from the sample, after the selected particle was already coated with protective carbon and Pt layers. (c) A final lamella can be seen, showing the cross-section of the selected particle supported on the substrate. 32

Figure 13: Schematic representation of multi-slice method. 35

Figure 14: STM micrograph of a chemically-treated single-crystal $SrTiO_3$ coated with 1 nm of conductive film, showing the terraces and ledges which have formed on the surface due to the BHF treatment. 37

Figure 15: Secondary electron SEM micrographs of (a) Pt particles dewetted on a (100)-$SrTiO_3$ substrate after annealing a 50nm thick Pt film at 1050ºC for 10 hours in Ar+2%O_2. (b) and (c) are inclined and plan-view micrographs of an equilibrated particle, where the increased density of $SrTiO_3$ steps is visible. 38

Figure 16: Parallel-Beamθ-2θ XRD pattern for Pt particles dewetted on a (100)-$SrTiO_3$ substrate. 41

Figure 17: In-plane XRD pole figure based on Pt (111) planes. The reflections are as follows: 1. (111)-Pt planes and (100) $SrTiO_3$ aligned parallel to the surface. 2. (111)-$SrTiO_3$ planes are inclined 55° from the (100)-$SrTiO_3$ (surface). 3. (111)-Pt planes are inclined 70.5° from the (111)-Pt (surface). 41

Figure 18: Secondary electron SEM micrographs of Pt particles at different stages of evaluation of ECS. Particle (a) is the furthest from reaching its equilibrium state, while particle (c) is the closest to the ECS. 43

Figure 19: (a) Bright field TEM micrograph of a cross-section view of a Pt particle equilibrated on the $SrTiO_3$ substrate. (b) Partial solution of the ECS of the particle presented in (a). (c) HRSEM plan-view micrograph of a typical Pt particle. (d) Simulation of the ECS of the Pt particle presented in (c) 44

Figure 20: (a) HAADF STEM micrograph of selected particle. The red square marks the area where the EDS spectrum (b) was taken from. 46

Figure 21: (a) Bright field diffraction contrast TEM micrograph of typical Pt particle equilibrated on a (100)-$SrTiO_3$ substrate (b) Electron diffraction from the particle and the substrate. 47

Figure 22:(a) An experimental HRTEM micrograph of the Pt/(100)-$SrTiO_3$ interface acquired at an objective lens defocus of -24 nm and a Cs of -7µm. (b) Bragg filtered image of the experimental micrograph presented in (a). 48

Figure 23: (a) HRTEM micrograph of the Pt-$SrTiO_3$ interface. (b) Atom positions in the $SrTiO_3$ at the region of (b) the interface, and (c) the bulk $SrTiO_3$. 49

Figure 24: HAADF STEM micrograph of the free surface of $SrTiO_3$ adjacent to a Pt particle.....50

Figure 25:(a) HAADF STEM micrograph of a $SrTiO_3$-Pt interface. (b) Magnified view of the interfacial area. (c) Line-scan intensity profile of the area marked in (a), showing the decaying HAADF signal (from the Pt to the $SrTiO_3$) at the interface.....51

Figure 26: TEM micrographs of Pt particles on planar amorphous SiO_2: (a)Predominantly hexagonal particles are observed following growth in N_2 at

600°C, (b)while exclusively squares and rectangles are observed following growth in H_2 [82].....52

Figure 27: (a) and (d) Experimental micrographs showing plan and side views of the Pt particle, respectively. The Pt particle is the same one as in Figure 19. (b) and (e) Simulations of the ECS of the Pt particle (plan and side view) presented in (a), based on the extracted experimental data. (c) and (f) Simulations of the ECS of the Pt particle presented in (a), whether it had reached a total equilibrium state. 56

Figure 28: Schematic drawing showing the source of error in determining the interface energy due to inclination of an equilibrated Pt particle on the $SrTiO_3$ substrate 58

List of Tables

Table 1: Physical properties of $SrTiO_3$ [54] 24

Table 2: Comparison of the experimentally determined Pt surface energy ratios to values from the literature. 55

Abstract

Thin continuous Pt films were evaporated on chemically treated (100)-$SrTiO_3$ single crystal substrates and then equilibrated in the solid-state. The equilibration took place at 1050°C and in the presence of an Ar/2%O_2 carrier gas mixture. Given the similar lattice parameters between Pt and $SrTiO_3$, a simple cube-on-cube orientation relationship was expected to form at equilibrium.

Following the thin film dewetting process, single crystal Pt particles were formed. While not all the particles reached their equilibrium state (shape), they all adopted the same general shape. X-ray diffraction analysis of the preferred orientation of the equilibrated Pt nano-particles showed that only a preferred orientation of Pt {111} parallel to the $SrTiO_3$ (100) surface formed, without a low-index orientation relationship.

The equilibrium crystal shape of the Pt particles and particle-substrate interfacial energy was analyzed using Winterbottom's approach and electron diffraction. It was found that the equilibrium crystal shape of the Pt particles, formed in the presence of oxygen, contains the following facets: {111}, {100}, {110} and {113}. In addition, the Pt-(100)-$SrTiO_3$ interfacial energy was determined to be 2.08 J/m^2.

High resolution electron microscopy (HRTEM and HRSTEM) was used to analyze the atomistic structure at the metal-oxide interface. It was found that reconstruction of

the $SrTiO_3$ surface (a complexion) took place, and this is believed to be responsible for the Pt texture after dewetting.

List of Symbols and Acronyms

γ	Surface energy
θ	Young's contact angle
ϕ	Equilibrium dihedral angle
f(p)	Confidence probability factor
k_{AB}	k-factor
n_0	Number of available atoms per unit area
n_i	Number of atoms undergoing some transition into or out of a particular energy state (kink, ledge, etc.)
Δt	Thickness of a thin slice
A	Surface area
$C_{lim(A)}$	Detection limit for element A in B
E	Energy
G	Gibbs free energy function
ΔG_S	Gibbs free energy per unit area
N	Counts
$P(O_2)$	Partial oxygen pressure
R	Gas constant
R_i/R_j	Radius vector
T	Temperature
Tm	Melting temperature
W_{ad}	Work of adhesion
2D	Two dimensions
3D	Three dimensions
CVD	Chemical vapor deposition

DI water	Deionized water
EBG	E-beam evaporation gun
EBSD	Electron backscattered diffraction
ECS	Equilibrium crystal shape
EDS	Energy-dispersive x-ray spectroscopy
EMS	Electron microscopy simulation
FCC	Face centered cubic
FIB	Focused ion beam
HAADF	High angle annular dark field
HREM-DIMA	High resolution electron microscopy - Digital image matching analysis
HRSEM	High resolution scanning electron microscope
HRSTEM	High resolution scanning transmitting electron microscope
HRTEM	High resolution transmitting electron microscope
IDIM	Iterative digital image matching
MBE	Molecular beam epitaxy
NCs	Nano-crystals
PB	Parallel beam
SEM	Scanning electron microscope
STEM	Scanning transmission electron microscope
STM	Scanning tunneling microscope
STO	$SrTiO_3$
TEM	Transmission electron microscope
TLK	Terrace ledge kink
UHV	Ultra high vacuum
XRD	X-ray diffraction

1. Introduction

Metal and metal oxide nano-particles are of interest of many modern applications such as catalysis, sensing, microelectronics, and memory devices. Nano-particles owe their special properties to the fact that a relatively large portion of the atoms are at, or near the surface. As a result, they often have novel electronic, optical, magnetic, chemical catalytic and mechanical properties compared to their bulk counterparts. Also, at this scale, quantum effects become dominant, which also lead to new sets of properties.

Many of the properties of such nano-crystals (NCs) are dictated by their thermodynamic state, including their equilibrium crystal shape, interface energy between the particle and the support material, surface reconstruction and/or structural relaxation at the interface, or the absorption of other atomic species. Many of these parameters depend on the processing conditions and environment the particles are exposed to. Because of their small size nano-particles are expected to reach a thermodynamic equilibrium shape after comparatively short times at moderate temperatures.

The aim of this research was to provide a better insight into nano-particles, by determining their equilibrium crystal shapes, measuring the interface energy between the particles and single crystal substrates, and by analyzing the atomistic structure at the interface (and surfaces). The idea was to combine the power of XRD, electron microscopy, advanced TEM image simulation, and statistical parameter estimation, together with Winterbottom analysis for surface and interface energy analysis in order

to obtain a better understanding of metallic nano-particles equilibrated on oxide substrates. Pt on (100) single crystal $SrTiO_3$ (STO) substrates was selected as a model system for this study, due to the fact that there is a very small lattice mismatch (~0.5%) between these two crystals and a cube-on-cube orientation was expected.

2. Literature Survey

2.1 Interfaces

The classical definition of an interface is a surface forming a common boundary among two different phases, such as in the case of two immiscible liquids, a liquid and a solid or a free surface. However, in the case of solid-solid interfaces, the interface can exist between a single phase, as in the case of the grain boundaries, as well as between two different phases.

Interfaces in general, and solid-solid interfaces in particular, play an important role in modern material systems, and are responsible for many of the electrical, optical, magnetic and mechanical properties. This is especially true for nano-scale systems, where relatively large portion of the atoms are at or near the interface.

2.1.1 Solid-Liquid Interfaces

Knowledge of the thermodynamic parameters of a material is important, since it potentially allows a better utilization and implementation of the material in various systems. In the case of liquid-solid systems, it is possible to extract interfacial thermodynamic data by conducting wetting (contact angle) experiments. In these experiments, a liquid drop is placed on solid surface, adopting a characteristic shape, which corresponds to the thermodynamic equilibrium between three phases, in the specific conditions. The real shape of a droplet depends on many factors, not all of them can be quantified [1], however it is acceptable to define the degree of wetting by its contact angle θ with a flat substrate (Figure 1). In the case when a liquid drop has

achieved thermodynamic equilibrium on a smooth, rigid, chemically homogeneous, insoluble, and non-reactive substrate [1,2], (Figure 1(a)), it is possible to determine the solid-liquid interfacial energy from Young's equation [3]:

$$\gamma_{SV} = \gamma_{SL} + \gamma_{LV}\cos\theta \tag{1}$$

where γ_{SV}, $\gamma_{LV}$and γ_{SL} are solid-vapor, liquid-vapor and solid-liquid interfacial energies respectively.

Another thermodynamic parameter which can be extracted from wetting experiments is the thermodynamic work of adhesion (W_{ad}), or the work per unit area which is required to separate an interface into two separate *equilibrated* free surfaces. It is possible to determine the work of adhesion based on the measured contact angle via the Young Dupree' equation:

$$W_{ad} = \gamma_{LV}\left(1+\cos\theta\right) \tag{2}$$

At elevated temperatures, diffusion processes often become dominant, causing mass transport and sometimes changes at the interface. The previously flat solid-liquid interface changes its morphology, resulting in the formation of dihedral angles at the triple junction (Figure 1(b)), which makes Young's equation not applicable. In this case, assuming the system has reached its equilibrium state and all the surface energies are isotropic, the relationship between the surface energies can be expressed via the Neumann equation [2,4]:

$$\frac{\gamma_{SL}}{\sin\phi_V} = \frac{\gamma_{SV}}{\sin\phi_L} = \frac{\gamma_{LV}}{\sin\phi_S} \tag{3}$$

where ϕ_V, ϕ_L and ϕ_S are equilibrium dihedral angles in the vapor, liquid and solid, respectively.

According to equation (3), if one of the surface energies is known, and dihedral angles were measured, the other surface energies can also be determined. However, the main challenge using Neumann's equations is to correctly determine and measure the dihedral angles. Therefore, a thorough morphological analysis is required [4,5]. In addition, Neumann's equation assumes an isotropic system, absent of torque.

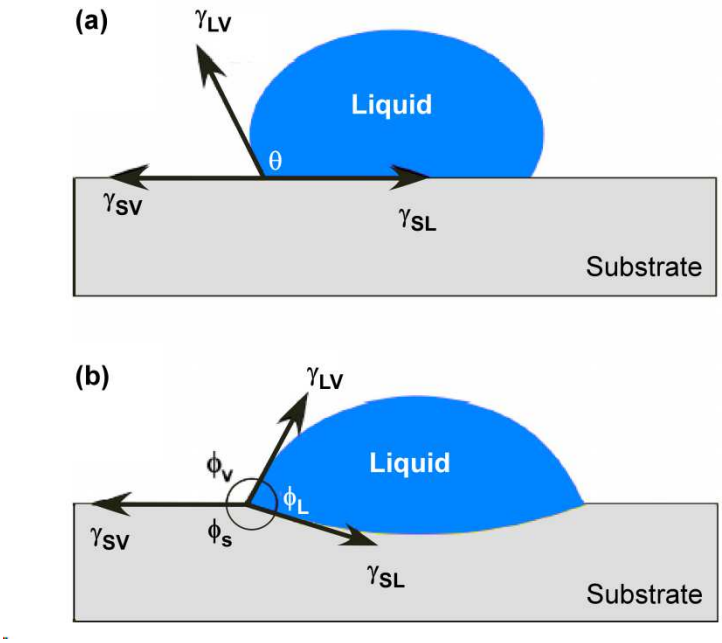

Figure 1: Schematic drawing of a liquid drop on a solid substrate. (a) The solid-liquid interface is flat and co-planar with the substrate (b) The solid-liquid interface is curved, forming a dihedral angle at the triple junction.

2.1.2 Solid-Solid Interfaces

The analysis of solid surfaces and solid-solid interfaces requires a different approach than that of liquids, since solid surface and interface energies can be anisotropic and have a facetted rather than a round equilibrium shape.

2.1.2.1 Macroscopic and Microscopic degrees of freedom

In order to define a grain boundary (or an interface) between two adjacent crystals five macroscopic and (at least) three microscopic degrees of freedom are needed [6]. Three of the five macroscopic degrees of freedom are used to define the orientation of one crystal with respect to the other (rotations), and two more are required to specify the orientation of the boundary plane with respect to one of the crystals. A schematic illustration of the macroscopic degrees of freedom is presented in Figure 2.

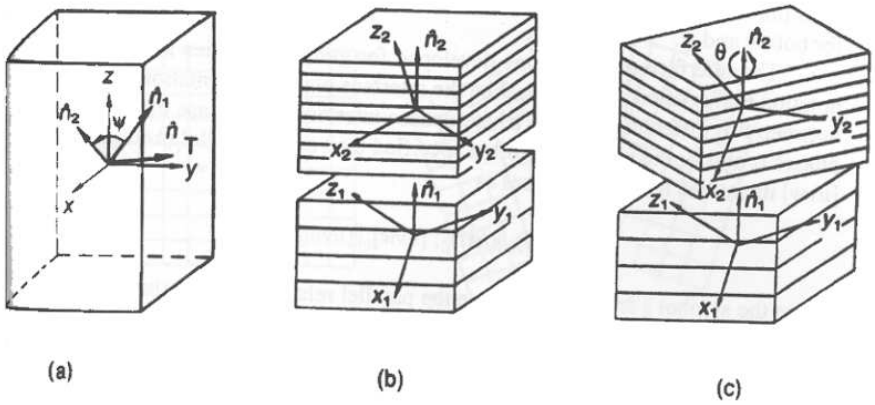

Figure 2: Illustration of the five macroscopic degrees of freedom of an arbitrary bicrystal interface. (a) The orientations of n_1, n_2 and n_r in a fixed coordinate system. (b) a tilt rotation of the two crystal coordinates systems so that n_1 is parallel to n_2, and (c) introduction of the twist component by rotating the top crystal n by the angle θ [7].

Microscopically, the three remaining degrees of freedom correspond to the translation vector of the two crystals composing the bicrystal [6]. However, since a wide variety of defects can form at the solid-solid interface, the amount of possible microscopic degrees of freedom is much larger, and as a result, quantitative treatment of interfacial phenomenon becomes more complicated. The microscopic degrees of freedom at the solid-solid interface include the translation of the atoms of both crystals, relaxation of

the interface, interface reconstruction, as well as dislocation or step formation and the boundary composition.

2.1.2.2 Degree of Coherency

Solid-solid interfaces between two phases are usually classified according to their degree of coherency (matching); interfaces with perfect lattice matching between two different crystals are called hetero-coherent interfaces. In this case, the lattice periodicity perfectly continues from one side of the interface to another without the slightest change or strain. In real life, hetero-coherent interfaces do not exist. There is always some mismatch between the two crystals. When the mismatch is small, the system prefers to maintain periodicity at the cost of creating elastic distortions (strain energy), which increases the general interfacial energy. When the mismatch is more significant, the distortions are also more significant. Dislocations or steps are formed at the interface to offset some of the coherency strain required to maintain the matching elsewhere. This type of interface is called a semi-coherent interface. When the degree of lattice mismatch between two crystals is large, what is called an incoherent interface is formed. In this case, there is no lattice matching.

2.1.2.3 Surface Reconstruction

Surface reconstruction refers to the process by which atoms at the surface of a crystal assume a different 2D structure than that of the bulk. Although reconstruction occurs at the upmost atomic layer of the bulk, the changes between the surface and the bulk structures cause strain which is expected to gradually fade over a few atomic layers, as schematically presented in Figure 3.

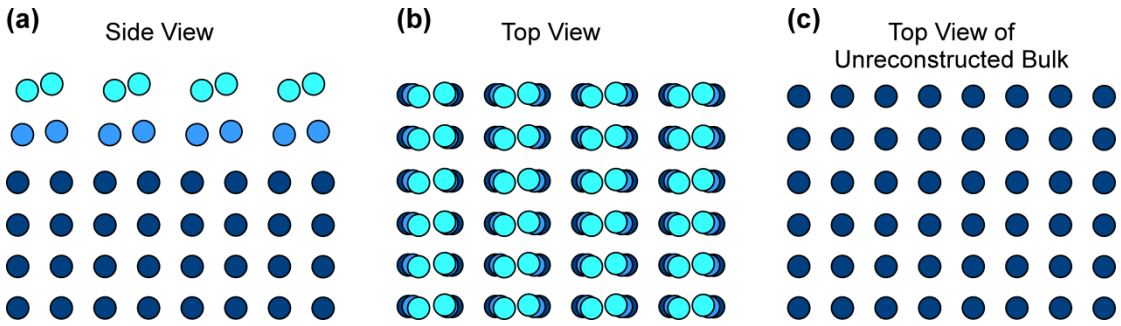

Figure 3: (a) Schematic drawing of the side view of a bulk phase with a reconstructed surface. The reconstruction at the top layer affects a few layers beneath it. (b) and (c) Schematic drawing of a top view of reconstructed and unreconstructed bulk accordingly.

Surface reconstruction is very prevalent in the nature. In fact almost every solid crystal undergoes surface reconstruction. The types of the reconstructions are diverse and are not constant per material, but rather depend on formation conditions (temperature, atmosphere, etc) [8,9,10]. One of the most famous examples of surface reconstruction is the 7x7 structure of the Si(111) surface [11,12,13]. For ideal Si(111), the basic unit which describes the surface structure is a hexagon, which is replaced with a rhombus domain, periodically repeated every 7x7unit cells.

2.1.2.4 Interface Reconstruction

Until recently, reconstruction had been predominately characterized at free surfaces and select grain boundaries. One of the first works to show that equilibrium reconstruction can also exist at interfaces was conducted by Meltzman et al. [14], who investigated equilibrated Ni particles supported on (0001) α-Al_2O_3 substrates. Due to the large lattice mismatch between these two materials, an incoherent interface was predicted. However, at equilibrium a periodic pattern was found at the interface, as

can be seen in Figure 4. The system decreased its interfacial energy by converting misfit strain at the interface to the new reconstructed structure ($2.5\sqrt{3}\ x\ 2.5\sqrt{3}R30$).

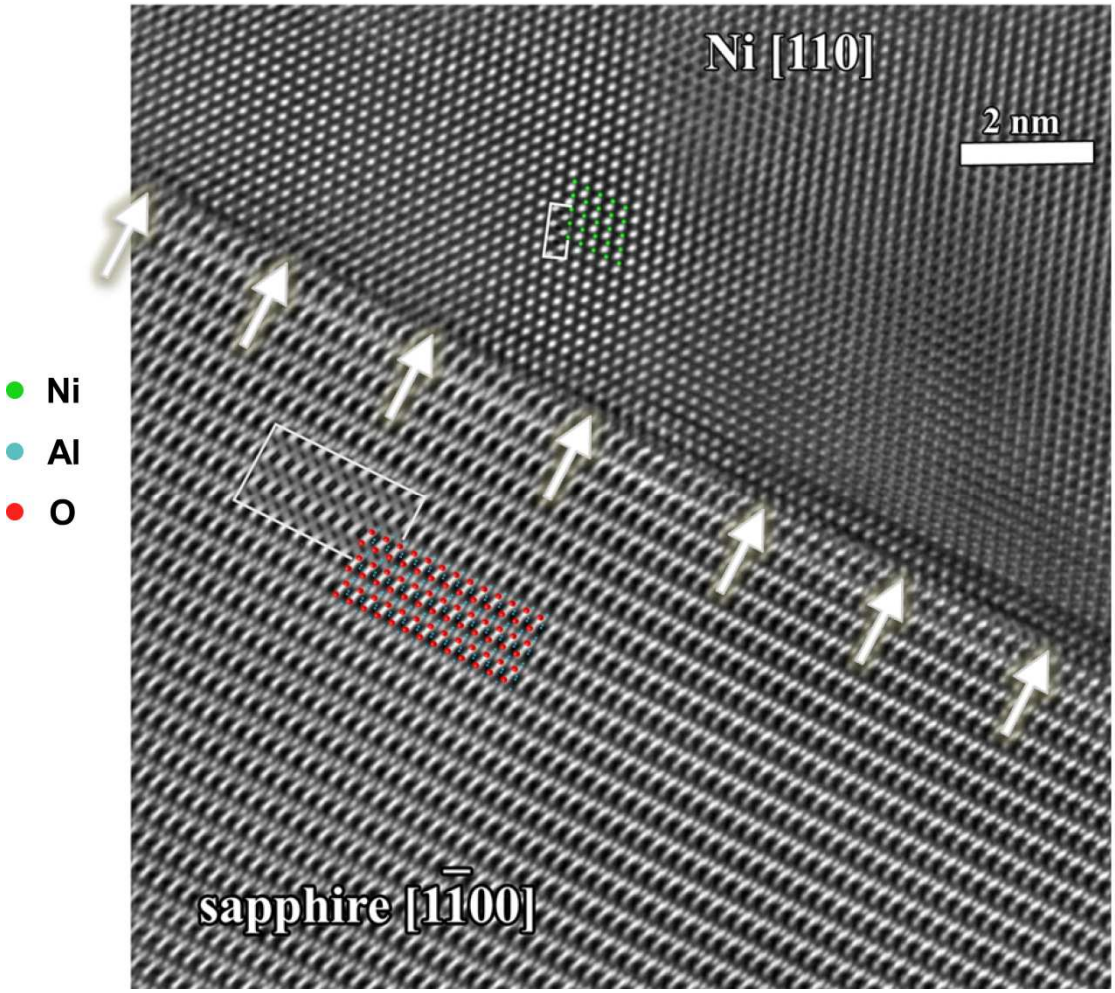

Figure 4: Phase contrast micrograph of the Ni–sapphire interface, showing periodic buckling of the of the terminating Ni layer (i.e. interface reconstruction) [14].

2.2 Solid State Dewetting

Continuous thin films are thermodynamically unstable. Solid state dewetting describes the rupture or agglomeration of a thin film (in the solid state) on a substrate and the formation of particles. Dewetting is driven by minimization of the total surface energy of the system. The dewetting process can be initiated simply by annealing a thin film at a high temperature, to activate diffusion. For solid state

dewetting the annealing temperature should be below the melting point of the film and the substrate. Dewetting can be used to equilibrate small particles on the substrate. Equilibrated particles can be used to study the equilibrium crystal shape (ECS) of the film material [28,15], and the interfacial energy between the film and the substrate [5,16].

The kinetics of the dewetting process depend on interface and surface transport mechanisms, and nucleation of the process may strongly depend on the nature and distribution of defects at the free surface, and at the interface between thin films and substrates [2]. There are two main mechanisms which are associated with the beginning of thin film dewetting; spinodal dewetting (Raleigh instability) and nucleation of voids [2,17].

Spinodal dewetting stands for the instability of thin films which results in wave fluctuations and the formation of surface curvatures which promote the rupture of thin films. These fluctuations are temperature dependent and increase with increasing thermal activation. In the case of solid-thin films, the rupture of the film will take place only if the amplitude of fluctuations is large enough to form hills and depressions via surface diffusion [2,17].

In polycrystalline films, solid-state dewetting is facilitated via the extension of grain boundary grooves from the free surface to the interface, or via nucleation of voids at the interface, and their extension to the free surface. In the case of film rupture via grain boundary groves, a polycrystalline film of thickness a, will rupture for the following conditions [18]:

$$\frac{R}{a} \geq \frac{3\sin^3\beta}{2-3\cos\beta+\cos^3\beta} \qquad (4)$$

where R is the grain size, and β is defined in terms the grain boundary (γ_{GB}) and surface (γ_{SV}) energies as $\beta = \sin^{-1}(\gamma_{GB}/\gamma_{SV})$.

No matter which mechanism dominates the rupture of thin films in solid-state dewetting, the end results of the dewetting process are the same; formation of a single crystal equilibrated particle on a substrate [2].

Rupture of a thin film leads to the formation of single crystal islands. Further annealing of these islands causes an evolution in shape, which ends in the equilibrium crystal shape (see chapter 2.3.1). At the initial stages of this process, the islands are usually asymmetrical and have almost the same height as the initial thickness of the film. However, governed by mass transport, these islands transform with time to symmetrical particles, which means an increase of the particle height at the expense of decreasing lateral radius. Since the shape evolution involves diffusion processes, this process is temperature dependent and related to the initial thickness of the film. As a result, the kinetics of dewetting increases with decreasing film thickness [2, 17]

2.2.1 Terrace Ledge Kink (TLK) Model

The TLK model describes the thermodynamics of crystal surface formation and transformation, as well as the energetics of surface defect formation. It originates from the works done by Kossel [19] and Stranski [20], and addresses idealized surfaces of elemental cubic crystals. Kossel defined defects on an elemental surface as terraces, ledges (steps) and kinks, as schematically described in Figure 5.

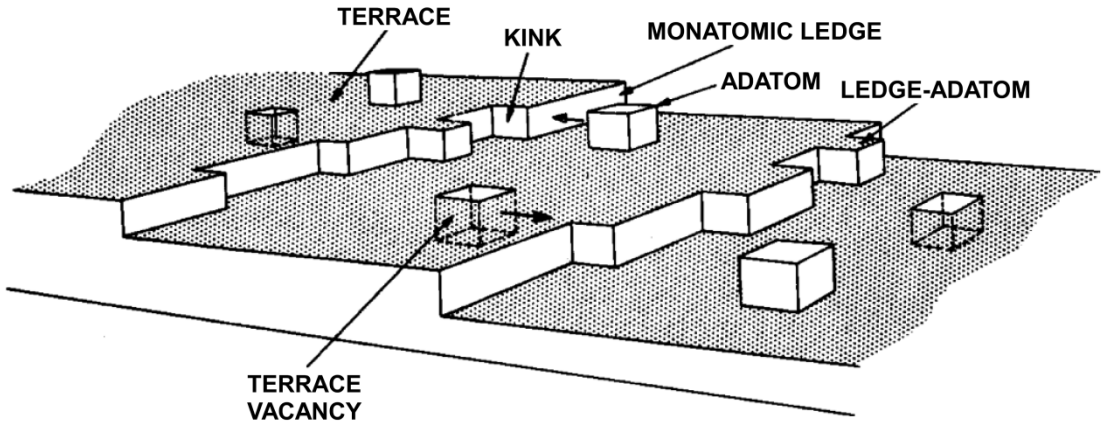

Figure 5: Model of a crystal surface showing monatomic height steps, kinks, single adatoms and terrace vacancies. Redrawn after Bonzel et al. [21]

According to the TLK model, all surfaces are categorized into three categories; singular, vicinal and rough surfaces [22]. Singular surfaces are the simplest of the three. They are considered to be smooth on an atomic scale, and correspond to surface orientations lying along a low index plane of the bulk lattice, e.g.(100), (110) and (111) planes of cubic crystals. Vicinal surfaces are considered to be made up of flat terraces of the closest singular orientation, separated by ledges of monatomic height, spaced so as to account for the surface orientation relative to a singular orientation. On vicinal surfaces that are misoriented in two directions relative to the singular orientation, the ledges will contain regularly spaced kinks, in order to accommodate the misorientation in the second direction. Rough surfaces are disordered surfaces on the atomic scale, even at a low temperature, to the extent that a description in terms of terraces, ledges and kinks is not possible anymore. Rough surfaces exist at equilibrium only above the roughening temperature [23].

The principal idea of the TLK model is that the energy of an atom's position on a crystal surface is determined by its bonding to nearest neighboring atoms and that

phase growth or transition simply involves the counting of broken and formed bonds. To add or remove an atom from a site and to move it somewhere else requires energy. In simple cubic, an atom in the crystalline bulk is bonded to as many as six nearest neighbors. Assuming that all the bonds are equal in this solid, to move an adatom to a kink site requires breaking one bond and making three new bonds at the kink site. The difference in energy in this process is the energy of two bonds. The change in the Gibbs free energy function (final state minus initial state) for this situation is:

$$\Delta G = E_{kink} - E_{adatom} \tag{5}$$

where E_{kink} and E_{adatom} are energies of kink atom and adatom respectively. Figure 6 displays a schematic energy diagram of different atomic sites of a simple cubic crystal. As can be seen from the diagram, the more an atom is surrounded by its neighbors, it is less energetic.

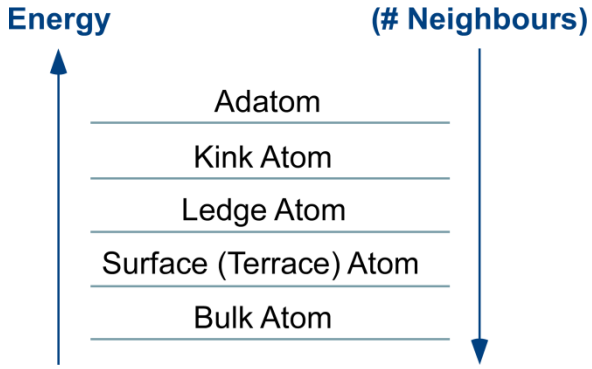

Figure 6: Schematic energy diagram of different atomic sites of a simple cubic crystal

As expected, the number of atoms undergoing some transition into or out of a particular energy state (kink, ledge, etc.) is dependent on the temperature and the number of such atoms available for that transition is:

$$n_i = n_0 \exp\left(-\frac{\Delta G_i}{RT}\right); \qquad i = \begin{cases} adatom \\ kink \\ \vdots \end{cases} \tag{6}$$

where n_0 is the number of available atoms per unit area.

According to the TLK model, crystal growth happens by atoms diffusing to less energetic sites, and thus minimizing the total energy of the system. For example, an adatom located on a terrace will diffuse to the nearest ledge, where it increases the amount of neighboring atoms, and from then it diffuses to its final site, the kink site. This way, a kink site is progressing, and a step is forming. When the kink reaches the end of the row, a new row is formed. This process continues until the system reaches its minimal energy state, the equilibrium state.

The TLK model was developed with the assumptions that atoms rigidly hold their positions, and therefore no relaxation or surface reconstruction occurs [22]. In addition, interactions with second or third nearest neighbors are not taken into consideration by this model.

2.3 Equilibrium Shape of Solids

The surface energy γ is defined as the reversible work required to create a unit area of surface under conditions of constant temperature, volume and chemical potential [24]. Gibbs showed that in order to reduce the total energy of the system, a minimization of the surface energy per area is required. For liquids, the surface energy is isotropic. As a result, liquid drops assume a spherical shape at equilibrium state (in the absence of external forces). For anisotropic solids, the surface energy is orientation dependent. For solids, the Gibbs free energy per unit area ΔG_S is defined as:

$$\Delta G_S = \sum_i \gamma_i A_i \tag{7}$$

where γ_i is the surface energy of the i^{th} crystal face, and A_i is the area of the face.

2.3.1 Wulff Construction

A theory determining the equilibrium shape of crystals was formulated by Wulff [25]. This theory assumes that the equilibrium shape of the crystal will be the one that minimizes the value of ΔG_S, under constriction of constant crystal volume, temperature and pressure. In general, Wullf's theorem states that for a crystal at equilibrium, there exists a point in the interior such that its radius vector R_i (perpendicular distance) from the i^{th} face is proportional to γ_i.

$$\frac{\gamma_1}{R_1} = \frac{\gamma_2}{R_2} = \ldots = \frac{\gamma_i}{R_i} = \text{Const.} \qquad \Rightarrow \qquad \frac{\gamma_i}{\gamma_j} = \frac{R_i}{R_j} \tag{8}$$

As derived from equation (8), if the ratio of surface energies is known, then the equilibrium crystal shape can be constructed. In the Wulff construction method, the surface energy is plotted in polar coordinates vs. the angle with respect to a particular direction (γ-plot). Planes are drawn perpendicular to the normal unit vectors at each point on the γ-plot. The inner envelope of the tangents corresponds to the equilibrium crystal shape with the lowest surface energy per a fixed volume. The typical Wulff construction (also known as the Wulff shape) is illustrated in Figure 7.

In general, a Wulff plot can have missing orientations, sharp edges and corners, and its facets can be rounded or flat. It should be noted that the γ-plot is temperature dependent, and as a result the ECS also changes with temperature. In general, with increasing temperature, the anisotropy of surface energy decreases, making ECS more spherical (or thermodynamically rough). Also, the model addresses only ideal single

crystals that have reached their equilibrium state. The crystal is assumed to be free of defects and stresses.

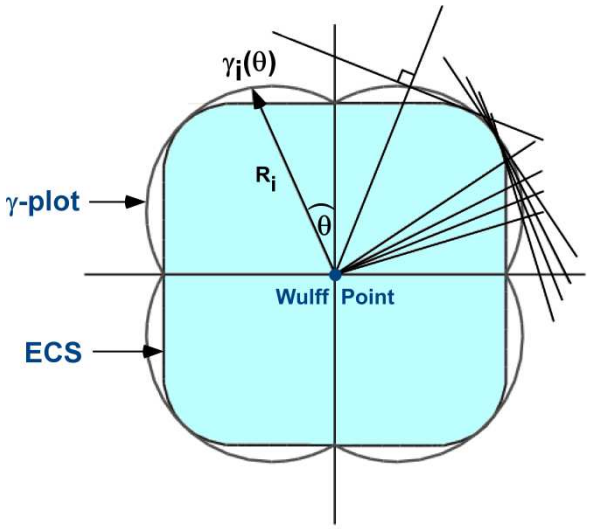

Figure 7: Schematic illustration of the Wulff construction, connecting the anisotropic surface free energy γ(θ), outer curve, with the equilibrium crystal shape function, inner curve (blue area).

2.3.2 Equilibrium Crystal Shape of a Solid Particle

The ECS of a particle reflects a characteristic shape which represents a total minimum of Gibbs' energy in the system. Therefore, based on the shape of the particle it is possible to determine surface and interfacial energies. Predicting the thermodynamic equilibrium (3D) shape of nano-particles (Wulff shape) is almost impossible to achieve since the exact surface chemistry is often unknown, and the impact of the changes in atomistic structure at the surface on the equilibrium crystal shape of particles is often ignored [26,27,28]. However, the ECS of equilibrated particles, and the solid-solid interface energy between the particles and flat substrates, can be experimentally determined.

2.3.2.1 Winterbottom Analysis

Winterbottom analysis is a relatively reliable method for measuring solid-solid interfacial energy [29]. According to this approach, for a system with a particle equilibrated on a flat substrate, and with a flat interface coplanar to the surface of the substrate, under conditions of constant temperature, volume and chemical potential, the equilibrium shape of the crystal will be the one that minimizes the value of ΔG_S (equation *(7)*), as was previously shown by Wulff for unsupported particles. For such a system, the interfacial energy can be determined by measuring two characteristic lengths in the Wulff shape: the distance from the center of the Wulff plot (Wulff point) to the interface with the substrate (R_1), and the distance from the Wulff point to a facet of the particle (R_2), as shown schematically in Figure 8:

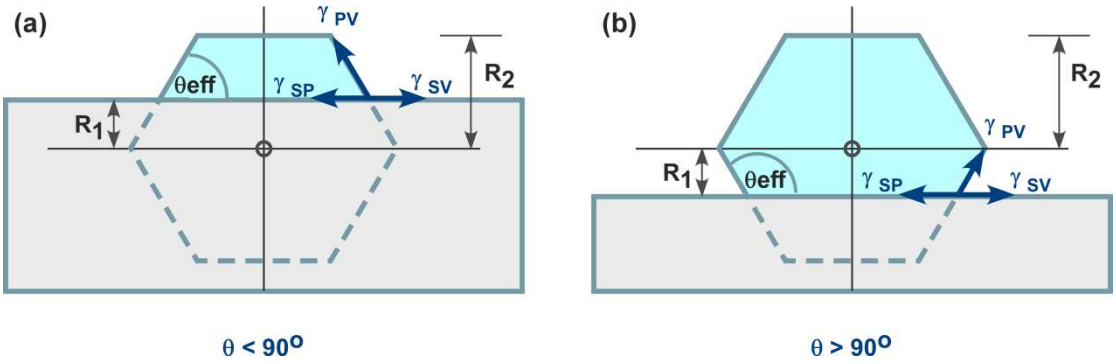

Figure 8: Schematic drawing of the Winterbottom analysis for particles equilibrated on a substrate with different effective contact angles; (a) $\theta < 90^0$ and (b) $\theta > 90^0$

For an effective contact angle larger than 90° (Figure 8(b)), measured values of R_1 and R_2 can be used to determine the interfacial energy according to:

$$\frac{R_1}{R_2} = \frac{\gamma_{sp} - \gamma_{sv}}{\gamma_{pv}} \qquad (9)$$

where γ_{sp} is the substrate-particle interfacial energy, γ_{sv} is the surface energy of the substrate, and γ_{pv} is the surface energy of the uppermost particle facet. For effect contact angles less than 90° this analysis requires at estimation of the position of the

Wulff point, potentially introducing large errors. For solid-solid interfaces, there is no meaning to use of the contact angle to determine the interface energy [2].

2.4 Pt-$SrTiO_3$ System

Metal-oxide interfaces, and specifically Pt-oxide interfaces, are important for a myriad of technological applications ranging from catalysis [30,31], fuel cells [32,33,34], sensing [35,36] and electronic materials systems [37,38,39,40,41]. Recently there is an increased interest in the Pt-$SrTiO_3$ system due to the small lattice mismatch at the room temperature between Pt (a_{Pt}=0.3920 Å)and $SrTiO_3$ (a_{SrTiO_3} = 0.3905 Å), which suggests that a hetero-epitaxial interface, desirable for various device applications, may be possible to obtain. This system is especially attractive for microelectronic [42,43], catalytic [31,44] and memory devices [45,46].

2.4.1 $SrTiO_3$

At room temperature, $SrTiO_3$ has a cubic perovskite structure (ABO_3) and it is often used as a model system for the entire perovskite family. In its stoichiometric form, single crystal $SrTiO_3$ is a chemically stable insulator, with a high dielectric constant (Table 1). It was found that optical, electrical, and magnetic properties of $SrTiO_3$ can be modified [47,48,49,50,51], which suggests flexibility in the material design and utility. In addition, $SrTiO_3$ is extensively used for epitaxial growth of oxide thin films [52,53]. All these together make $SrTiO_3$ a very attractive material for many modern applications.

Table 1: Physical properties of $SrTiO_3$ [54]

Properties	**Value**
Density:	5.1 g/cm³
Molar Mass:	183.49 g/mol
Melting Point:	2080 °C
Crystal Structure:	Perovskite
Space Group:	Pm3m
Thermal Expansion:	$9x10^{-6}$ 1/K
Dielectric Constant:	332
Band gap (T=0K):	~3.2 eV

The $SrTiO_3$ unit cell is presented schematically in Figure 9(a) and it is composed of a single Ti^{+4} cation positioned in the center of the cubic cell, eight Sr^{2+} cations positioned at the corners of the cube and six O^{2-} anions occupying the center of the cube facets. In this way, each unit cell is composed of one strontium, one titanium and three oxygen atoms. When looking at $SrTiO_3$ from <001> direction, its structure can be described as being composed of alternating layers of TiO_2 and SrO layers (Figure 9(b)). Both these surfaces are nonpolar, but have a different chemistry: SrO is a basic oxide while TiO_2 is acidic [66]. Heifets et al. calculated surface energies for both these (unreconstructed) terminations and found them to be very similar, which suggests that both terminations can coexist, having an average surface energy of 1.32 J/m^2 [55]. Other groups also showed that both surfaces have a comparable range of thermodynamic stability, which implies that (100)-$SrTiO_3$ can be either SrO or TiO_2-terminated, depending on the growth conditions. The average surface energy for the (1x1) unreconstructed surface was calculated to be 1.36 J/m^2 and 1.46 J/m^2 by Padilla et al. [56] and Johnston et al. [57], respectively.

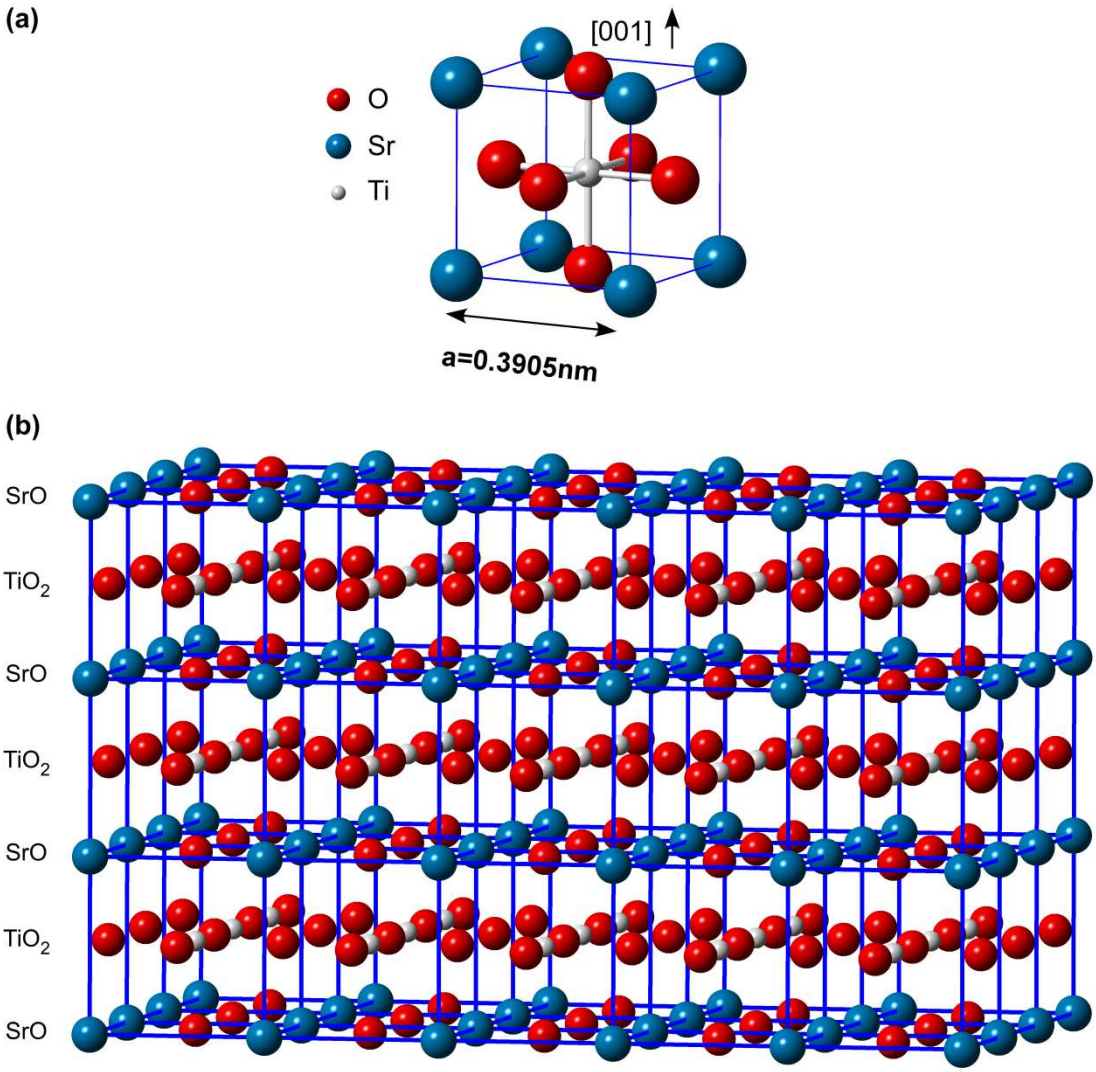

Figure 9: (a) $SrTiO_3$ cubic unit cell. (b) A 3D view of $SrTiO_3$ structure from <001> direction, showing alternative atomic layers of the TiO_2 and SrO in the cubic structure.

2.4.2 Pt-$SrTiO_3$ System

Various highly oriented Pt films have been fabricated on (100)-$SrTiO_3$ substrates by molecular beam epitaxy (MBE), sputtering, laser deposition, and other techniques. It was noticed that the substrate temperature during film deposition can have a major influence on the morphological characteristics of the Pt film [58,59]. For lower temperatures, a {111}-texture was dominant for Pt on $SrTiO_3$, while for higher deposition temperatures formation of a low-index orientation relationship was found

to depend on the substrate morphology [59]. Son et al. reported that annealing the $SrTiO_3$ substrate in O_2 (prior to Pt deposition) and deposition at a sufficiently high temperature contributes to {100} oriented growth of Pt on (100)-$SrTiO_3$ [59]. They suggested that higher temperatures favor {100}-textured films because the surface energy anisotropy decreases with increasing temperature, allowing for stabilization of the {100} orientation, while annealing the substrate in an oxygen-rich atmosphere removes surface impurities and thus prevents nucleation of {111} oriented Pt grains. Other works suggested that by removing impurities from the Pt target (rather than from the substrate), nucleation of {111} oriented Pt grains can be prevented [60,61]. Goto et al. reported that increasing the oxygen concentration in the carrier gas during chemical vapor deposition (CVD) of Pt removed organic contaminants, resulting in an increased degree of {111} texture on various oxide surfaces [62].

In contrast, simulations of the stability and adhesion of Pt on the (100)-$SrTiO_3$ surface showed that the interface with TiO_2-terminated $SrTiO_3$ is significantly more stable than with SrO-terminated $SrTiO_3$ [63,64]. This is in agreement with the experimental work by Polli and coworkers which showed that SrO termination of (100)-$SrTiO_3$ promotes {111} texture, while TiO_2 termination enables the formation of a low-index cube-on-cube orientation relationship of Pt on $SrTiO_3$, suggesting stronger interactions between Pt and TiO_2 [65].

The fact that Pt seems to favor one type of termination over the other, despite the similarity in surface energies of both (1x1)-unreconstructed terminations, may indicate that the Pt/(100)-$SrTiO_3$ interface is more complex than originally perceived, and further investigation is warranted. This statement is reinforced by the fact that

most of the studies have been theoretical in nature, and most of the experimental works have not studied fully equilibrated Pt-$SrTiO_3$ interfaces. In fact, it was reported by Erdman et al. that different annealing conditions result in different $SrTiO_3$ surface reconstruction [8], which in turn, can affect the macroscopic and microscopic degrees of freedom of the Pt-$SrTiO_3$ system. In the present study, solid-state dewetting at a defined oxygen partial pressure of continuous Pt films on (100)-$SrTiO_3$ was used to form equilibrated Pt particles in contact with $SrTiO_3$, for subsequent experimental characterization of the Pt shape and relative orientation with the substrate.

2.5 Research Goals

The objective of this research was to provide a better insight into nano-particles, by determining their equilibrium crystal shapes, measuring the interface energy between the particles and single crystal substrates, and by determining the atomistic structure at the interface (and surfaces). The idea was to combine the power of electron microscopy together with advanced image simulations, as well as other characteristic methods in order to extract thermodynamic data for metallic nano-particles equilibrated on substrates.

Pt on $SrTiO_3$ was selected as a model system for this study, due to the small lattice mismatch at the room temperature between Pt and $SrTiO_3$ (less than 0.5%), which suggests that a hetero epitaxial interface, desirable for various device applications, may be possible to obtain.

The goal of the research was to conduct a thorough thermodynamic analysis on Pt particles equilibrated on (100) $SrTiO_3$ substrates. The specific research goals were:

- To characterize the system morphology and structure, following the equilibration (dewetting) process.
- To characterize the ECS of the Pt particles formed at a relatively high $P(O_2)$.
- To determine the particle-substrate orientation relationship.
- To determine the particle-substrate interfacial energy.
- To characterize the Pt-$SrTiO_3$ interface structure at the atomistic level.

3. Experimental Methods

3.1 Sample Preparation

3.1.1 Substrate Preparation

Polished single crystal (100)-$SrTiO_3$ substrates of 99.99% purity, with a miscut angle < 0.5° and a roughness less than 0.5nm, were provided by Crystal GmbH. The substrates were first rinsed in DI water in an ultrasonic bath, and then chemically wet-etched in an ammonium fluoride buffered HF mixture (NH_4F 35.6%, HF 6.4%, pH ~ 4.5) for about 30 seconds. The substrates were then rinsed again with DI water and dried under flowing N_2. After chemical etching, the substrates were annealed in air at 950°C for 2 hours. This treatment procedure was previously shown to be effective for producing high-quality (100)-$SrTiO_3$ surfaces terminated with TiO_2 [66,67,68].

3.1.2 Pt Film Deposition

Post treatment, 50 nm thick Pt films were deposited on the substrates. The film thickness was chosen to be 50 nm, since it produced large enough equilibrated particles to be handled by FIB, so TEM specimens could be prepared, but small enough so the particles could reach equilibrium in a reasonable period of time (and temperature). The Pt films were deposited by e-beam evaporation, which is schematically presented in Figure 10. The general principle is as follows; the Pt target (the source) is heated up under high vacuum conditions ($2x10^{-7}$ Torr) by the electron beam which is extracted from the filament and deflected towards the target by magnets. Under heating, the Pt evaporates and reaches the $SrTiO_3$ substrates, at a

deposition rate of ~0.1-0.2 Å/sec. During deposition the substrates were at ambient temperature.

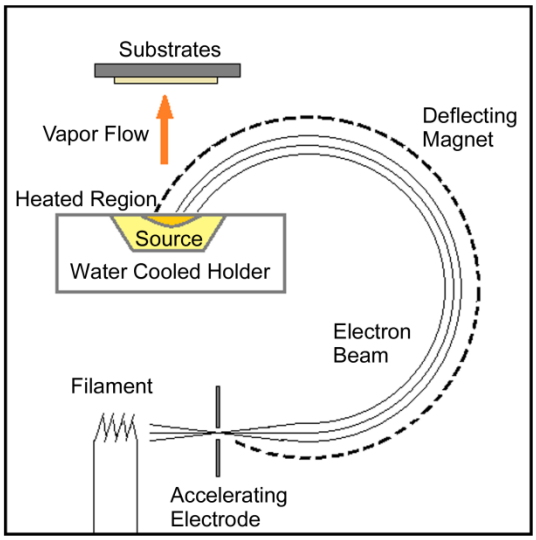

Figure 10: Schematic drawing of EBG evaporation system

3.1.3 Dewetting Experiments

Following film deposition, the specimens were annealed at 1050°C (0.65Tm of Pt) to promote solid-state dewetting in order to produce a large number of Pt NCs. The process was conducted in a furnace, constructed of a set of sapphire tubes that were assembled inside a conventional polycrystalline alumina-tube. This way, the specimens, which were placed inside the inner sapphire tube, were isolated from external impurities, as well as internal impurities originating from the alumina tube. A schematic drawing of this experimental setup is shown in Figure 11.

The annealing process was conducted in a gas mixture of Ar + 2% O_2 (99.99% purity) at 1050°C for 10 hours, followed by cooling at a rate of ~8°C/min. A dewetting time of 10 hours was selected because, on the one hand, it resulted in small particles with facets of the same family having equal lengths, indicating an equilibrium shape, and

on the other hand it was short enough so no significant evaporation of the Pt and $SrTiO_3$ could take place. The annealing process was conducted in the presence of oxygen in order to prevent the formation of aninterfacial phase between the particles and the substrate [69]. The partial pressure of oxygen ($P(O_2)$) during the annealing process was measured using a zirconia oxygen detector located at the gas exit-port of the furnace. The measured $P(O_2)$ was $1.5x10^{-3}$ atm.

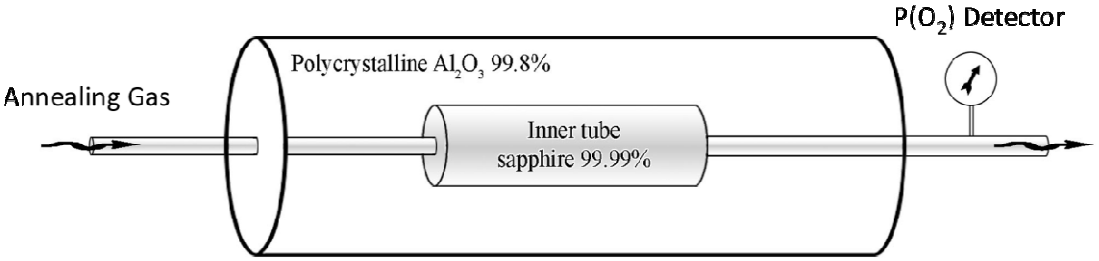

Figure 11: Schematic drawing of experimental setup of dewetting experiments

3.1.4 Focused Ion Beam (FIB)

Site-specific transmission electron microscopy (TEM) specimens of the Pt-$SrTiO_3$ interface were prepared using a dual-beam focused ion beam (FIB; Strata 400s, FEI) using the lift-out technique [70,71]. The selected particles (single-crystals close to equilibrium state) were first coated with a ~80-150nm thick carbon layer, followed by a thin Pt film, which was used to prevent surface damage during subsequent FIB milling. The carbon film was used to clearly differentiate the Pt particles from the Pt protective film as well as for alignment of the aberration corrector during subsequent TEM work. Then, using a Ga+ ion beam, a lamella was cut and attached to the Mo grid using an OMNIPROBE^{TM}, followed by the final polishing and thinning of the specimen. Each of the produced lamellas was around 15-20 µm wide, 10 µm height and 30-100 nm thick and contained only one particle of interest (Figure 12(c)).

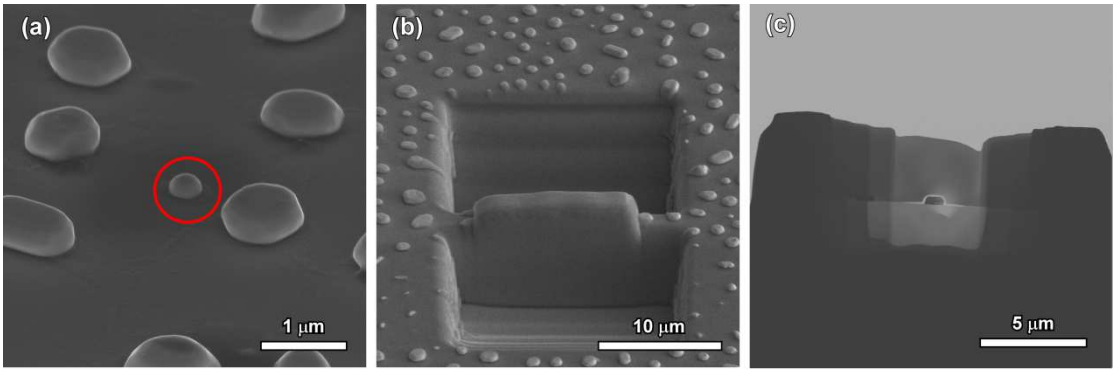

Figure 12: SEM micrographs showing different stages of TEM sample preparation by FIB. (a) A plan-view of selected particle supported on the substrate. (b) This micrograph shows the process of milling a lamella from the sample, after the selected particle was already coated with protective carbon and Pt layers. (c) A final lamella can be seen, showing the cross-section of the selected particle supported on the substrate.

3.2 Characterization Methods

3.2.1 X-Ray Diffraction (XRD)

XRD analysis was performed using a Rikagu Smart Lab X-Ray Diffractometer with CuKα radiation, at an accelerating voltage of 45kV and anode current of 200 mA. The preferred orientation of the particles with respect to the substrate was determined by θ-2θ parallel beam (PB) measurements, while 2θ angles range was 20-100° with a step size of 0.01°. Monochromatization of the beam was achieved using a two-crystal monochromator (PB-Ge(220)x2). The in-plane preferred orientation of the particles was examined by in-plane pole-figure measurements, with a diffraction angle of 39.7634° which corresponds to the Bragg angle of Pt (111) planes. Prior to pole-figure measurements, slit collimation was done as well as precise alignment of the sample was performed using rocking curves on the STO (200) reflection.

3.2.2 Scanning Electron Microscopy

The morphology of the equilibrated particles, supported on the substrate, and morphology of the substrate were examined using high resolution scanning electron microscopy (HRSEM; Zeiss Ultra-Plus FEG-SEM). The acceleration voltage ranged from 2 to 6 kV. Most of the micrographs were acquired using secondary electrons from an (in-lens) detector, at 3-4 mm working distance.

For conducting preferred texture analysis, electron backscattered diffraction (EBSD) analysis was performed, using an acquisition system (Oxford Instruments, UK) mounted on a FEI Quanta 200 environmental SEM. EBSD measurements were conducted at 20 kV with a ~4.5nA electron-probe current, at a 20 mm working distance.

3.2.3 Transmission Electron Microscopy

High resolution TEM (HRTEM) micrographs of the samples were acquired using a monochromated and aberration corrected FEI Titan 80-300kV S/TEM, operated at 300 kV. This microscope has a coincident point-to-point resolution and information limit of 0.07 nm and a focal spread of 3 nm (at 300 kV). This microscope was also used to conduct chemical analysis of the particle composition. This analysis was conducted using high angle annular dark field (HAADF) scanning transmission electron microscopy (STEM)

Prior to HRTEM, the samples were first cleaned with a low energy, reactive gas plasma, generated with a gas mixture of 25% oxygen and 75% argon, in a Fischione Plasma Cleaner (Model 1020). This process was conducted in order to remove

organic contamination, mainly hydrocarbons, and thus improve the quality of the specimen.

Electron diffraction, required for determining the particle-substrate orientation relationship, was conducted using a Tecnai G^2 T20 TEM microscope, operated at 200 kV.

3.2.4 Scanning Tunneling Microscope (STM)

Variable temperature UHV STM from Omicron was used to visualize the surface of the treated substrate. The STM device was operating at constant current mode of 1200 pA and at accelerating voltage around 1.2V.

3.2.5 Simulations

3.2.5.1 Image Simulations

HRTEM micrographs are formed due to passage of the incident electron beam through the crystalline structure (specimen) and TEM column. However, due to the microscope and specimen imperfections, some loss and even distortion of the information compared to the real structure occurs. To analyze the differences between the experimental micrograph and the real structure, and understand their impact on image interpretation, image simulation was conducted.

3.2.5.1.1 Electron Microscopy Simulation (EMS) Software

HRTEM simulations were generated using EMS software, developed by Stadelmann [72]. EMS is based on the multi-slice method, which is based on the idea of slicing a

specimen of thickness t into many thin slices of thickness Δt, in the direction of the incident beam [73], as can be seen in Figure 13. For each slice, the potential is projected onto a plane and the corresponding projected potential is calculated. The propagation of the electron wave from the exit surface of one slice to the incident surface of the next slice (over a distance Δt) is considered as Fresnel propagation in vacuum. The final exit wave is obtained when all the slices have been taken into account.

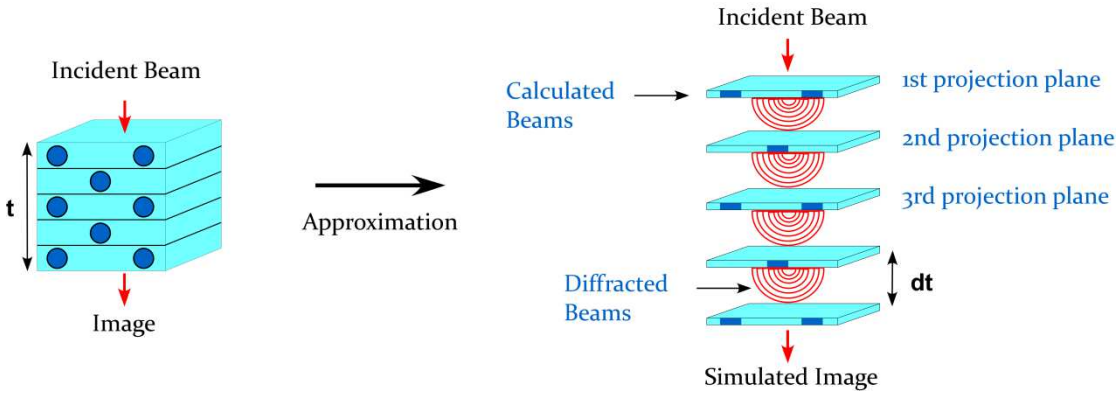

Figure 13: Schematic representation of multi-slice method.

3.2.5.1.2 High Resolution Electron Microscopy Digital Image Matching Analysis (HREM DIMA)

Quantitative analysis of the HRTEM micrographs was conducted by automated comparison of experimental micrographs and simulated images using HREM DIMA software, developed by Kaufmann [74]. This software is based on the principle of iterative digital image matching (IDIM) [75], which is the comparison of the experimental micrograph contrast to the simulated images, generated using EMS [72]. This approach allows to extract quantitative information from a single experimental HRTEM micrograph and to very precisely determine the exact conditions at which the experimental data was acquired (objective lens defocus and thickness of the

specimen), and ultimately the positions of the projected atomic columns in the specimen.

3.2.5.2 Equilibrium Crystal Shape Simulations

Equilibrium Wulff Shape Generator software (also known as Wulffman software) was used to simulate the shape of equilibrated particles, based on the measured facet areas [76]. Wulffman is an interactive online program which visualizes a 3D crystal shape based on the Wulff shape construction method [25]. To plot the crystal shape, this software requires the point group symmetry of a crystal, a set of crystal planes (facets) and their respective surface energies. Any change in data is automatically reflected in the presented crystal shape.

4. Results

4.1 $SrTiO_3$ Morphology After BHF Treatment

The surface morphology of the treated substrate was examined using STM. Prior to STM analysis the treated substrate was first coated with 1 nm of conductive Pt film in order to improve its conductivity. The STM analysis showed that after the chemical treatment in the BHF mixture solution, the (100)-$SrTiO_3$ single crystal substrate exhibited a surface morphology consisting of terraces and ledges as can be seen from in Figure 14.

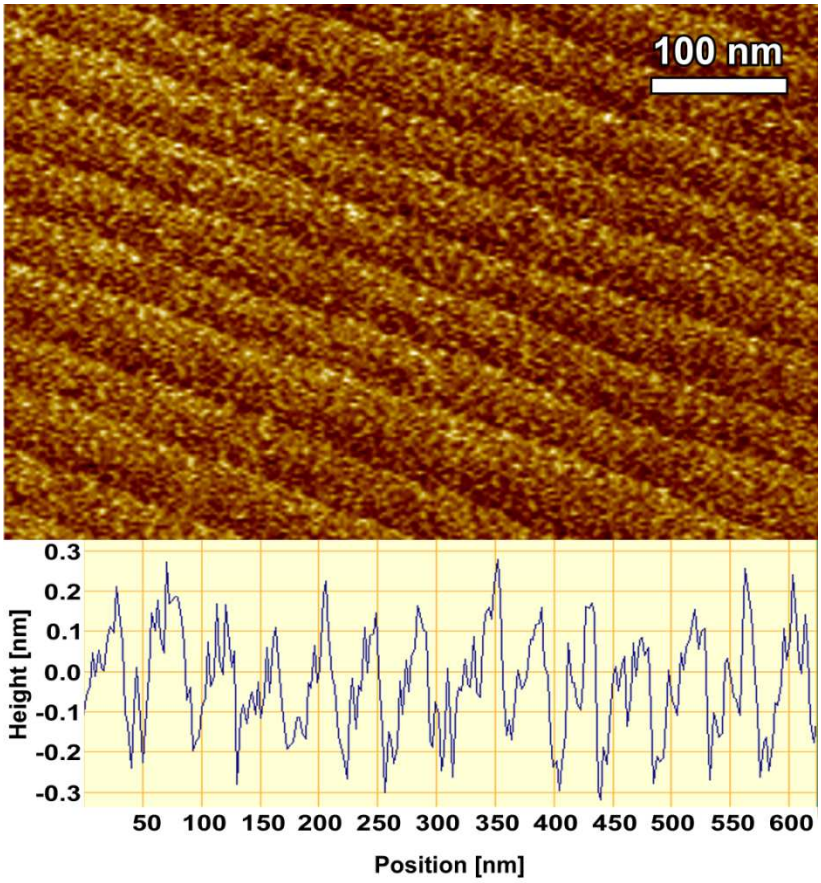

Figure 14: STM micrograph of a chemically-treated single-crystal $SrTiO_3$ coated with 1 nm of conductive film, showing the terraces and ledges which have formed on the surface due to the BHF treatment.

In the examined area, all the terraces are about the same height of 0.4 nm, which is the height of the unit cell of $SrTiO_3$, as expected after the BHF treatment [66,67,68].

4.2 Dewetting Results

Pt particles were formed by dewetting Pt thin films on the $SrTiO_3$ substrates in an oxygen rich environment (Figure 15). After the dewetting process, the substrates exhibited a certain degree of roughness, which implies that some evaporation took place together with retraction of the Pt film.

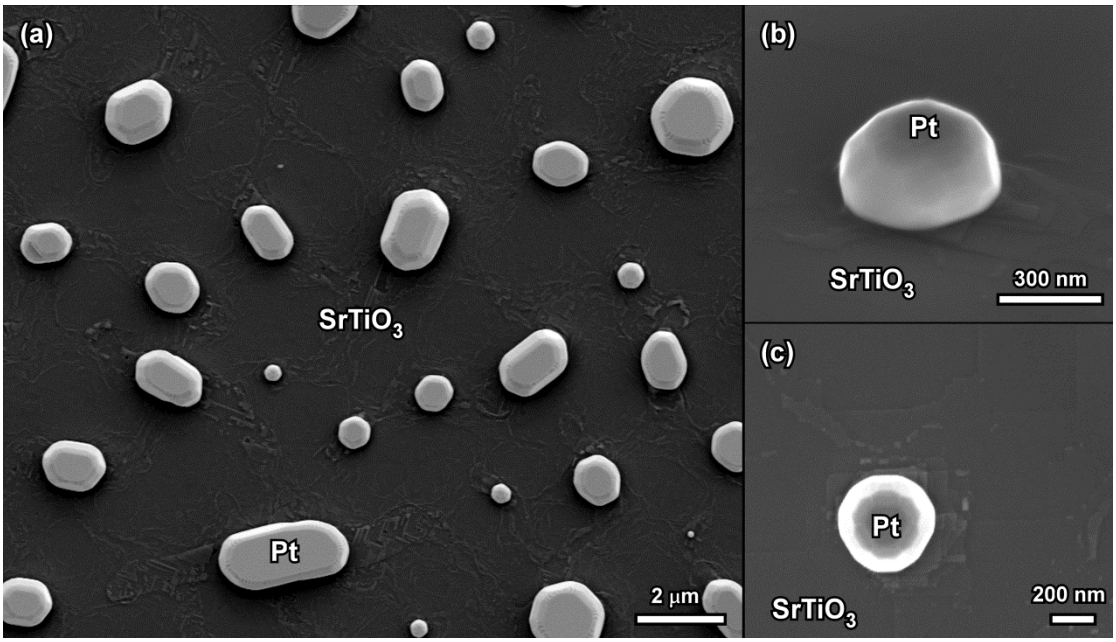

Figure 15: Secondary electron SEM micrographs of (a) Pt particles dewetted on a (100)-$SrTiO_3$ substrate after annealing a 50nm thick Pt film at 1050ºC for 10 hours in Ar+2%O_2. (b) and (c) are inclined and plan-view micrographs of an equilibrated particle, where the increased density of $SrTiO_3$ steps is visible.

The average size (diameter) of the single crystal particles was about one micron, while only particles below 400 nm reached an equilibrium state (shape). Variation in the particle shapes (and heights), including the presence of bi-crystals, was observed, although all the particles exhibited the same general form, which suggests different

stages of evolution of the ECS. Particles which were further from equilibrium were more elongated and more flat, while particles which were closer to their equilibrium state were more equiaxed. It should be noted that in addition to the prevalent case where the substrate forms ridges around the particle [77], the particles were positioned above the mean substrate plane (Figure 15(b)), on newly created $SrTiO_3$ steps, and small ridges formed at the triple junction (less than ~20nm in height).

4.3 Pt-$SrTiO_3$ Orientation Relationship

Figure 16 presents XRD results for Pt particles equilibrated on a single crystal (100)-$SrTiO_3$ substrate. Since Pt and $SrTiO_3$ both have cubic structures with very similar lattice parameters, their XRD reflections coincide, especially for low-index planes. For that reason, the reflections acquired in Parallel-Beam θ-2θ analysis theoretically could belong to both the particles and the substrate. However, since the substrate is a single crystal and Pt has a FCC structure, the only uncertainty is whether the (200) Pt reflections are masked behind (200) $SrTiO_3$ reflections. Particles having (200) planes parallel to the surface have a distinctive shape, which can be recognized using HRSEM. However, such particles were not detected by HRSEM or by electron backscattered diffraction (EBSD) analysis. Therefore it was concluded that the majority of equilibrated or nearly equilibrated Pt particles were oriented with the (111) plane parallel to the (100)-$SrTiO_3$ substrate, which means that a cube-on cube orientation relationship was not formed.

Pole figure analysis was conducted to study the in-plane particle-substrate preferred orientation. First, the samples were aligned according to STO (200) planes, which are parallel to the surface, and then the measurements were conducted with a diffraction

angle of 39.7634° which corresponds to the Bragg angle of Pt (111) planes and very close to the Bragg angle of STO (111) planes (2θ = 39.9842°). The pole figure results are displayed in Figure 17, showing three sets of reflections, marked as 1, 2 and 3. The first reflection is from (111)-Pt planes which are aligned parallel to (100)-$SrTiO_3$ and accordingly to the surface. The second set of 4 reflections belongs to (111)-$SrTiO_3$ planes which are inclined 55° from the (100)-$SrTiO_3$ (surface). The third set of reflections belongs to (111)-Pt planes, which are inclined 70.5° from the (111)-Pt (surface). However, as can be seen from Figure 17, the third set of reflections is constructed of two types of reflections, periodically observed every 30°; i.e. broad peaks separated by narrow peaks. This periodicity of 30° is somewhat expected since for the current projection; Pt (111) planes have a three-fold symmetry, and STO (100) have a four-fold symmetry, combined to give a periodicity of 360°/12 = 30°. However, the reason for two types of reflection remains unknown. In addition, close inspection of the 3rd set of reflections show a slight inclination of the circle with respect to the pole figure center, which indicates that the Pt (111) planes are almost but not really parallel to the surface (STO (100)). There is no clear explanation for this phenomena, although the presence of substrate steps beneath the particles may contribute to this behavior.

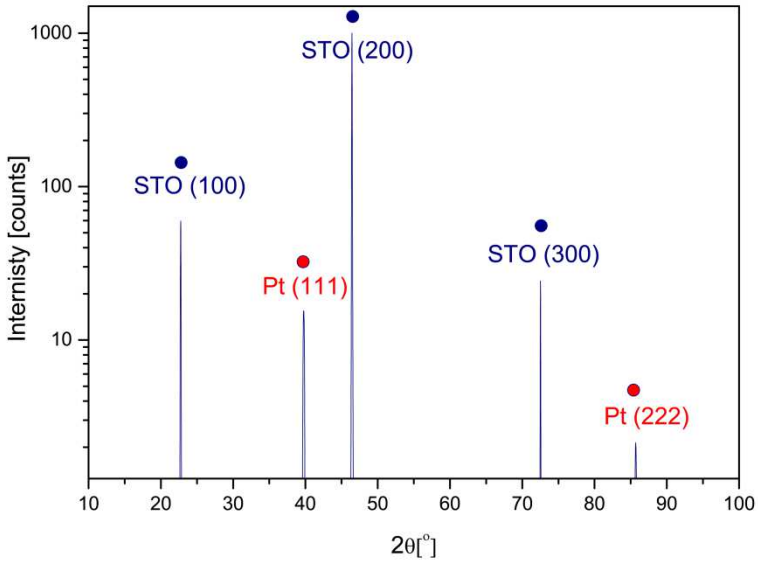

Figure 16: Parallel-Beam θ-2θ XRD pattern for Pt particles dewetted on a (100)-$SrTiO_3$ substrate.

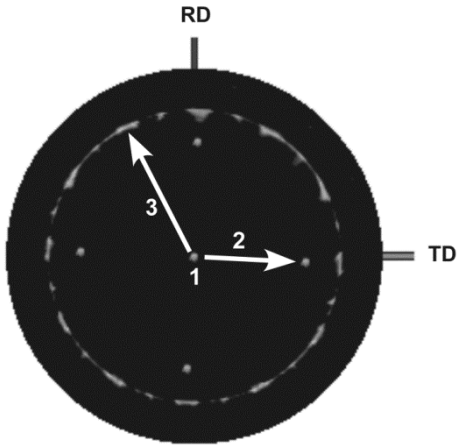

Figure 17: In-plane XRD pole figure based on Pt (111) planes. The reflections are as follows: 1. (111)-Pt planes and (100) $SrTiO_3$ aligned parallel to the surface. 2. (111)-$SrTiO_3$ planes are inclined 55° from the (100)-$SrTiO_3$ (surface). 3. (111)-Pt planes are inclined 70.5° from the (111)-Pt (surface).

Cross-section TEM from equilibrated particles (using several different zone axes) confirmed that there is a preferred orientation of Pt (111) parallel to the $SrTiO_3$ (100) surface, but in many cases the Pt (111) planes were slightly inclined relative to the

(100) substrate planes. The TEM analysis confirmed that there is a degree of isotropy about the (111) preferred orientation.

4.4 ECS of Pt

Figure 18 shows three different particles formed during the same dewetting process. The particles differ in shape and height and represent different stages of evolution of the ECS. The particle in Figure 18(a) represents the stage when the particle begins to exhibit the general form of the ECS; all the main facets can be detected, but the particle is elongated, relatively flat and not equiaxed. In addition, facets from the same family differ in area and geometry. The particle in Figure 18(b) is an evolution of the particle in Figure 18(a). It is less elongated, higher and more equiaxed. Figure 18(c) shows a particle in the final stage of reaching its ECS. The particle has the highest symmetry and facets of the same family are similar in size. In addition, its shape resembles a truncated (and faceted) sphere. Also, particles (a) and (b) in Figure 18exhibit steps on certain types of the facets, which implies that the particles haven't reached their ECS and that the growth mechanism of these particles is follows the TLK model. Particle (c) in Figure 18 doesn't exhibit the same steps which might suggest that the relevant facets have reached their final equilibrium state.

In Figure 18 (and some following figures) some facets exhibit some protrusions. It is important to emphasize that these defects are not part of the particles' ECS, which had perfectly smooth facets after their formation, but rather impurities accumulated during SEM specimen preparation.

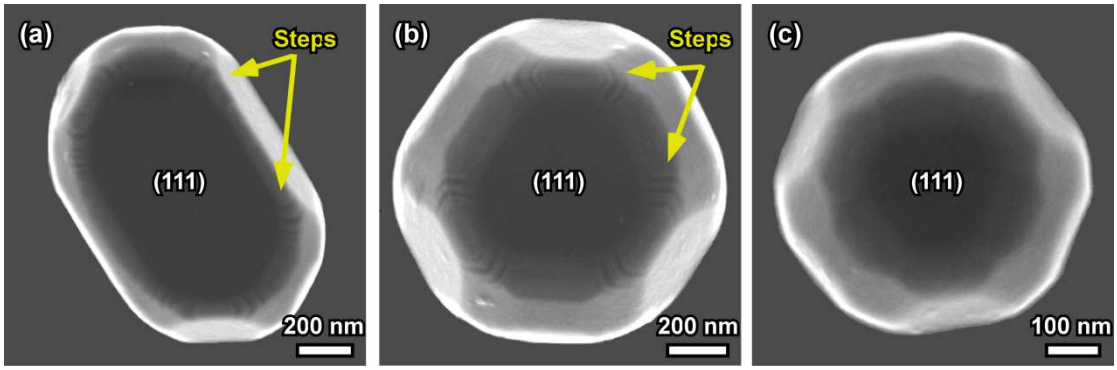

Figure 18: Secondary electron SEM micrographs of Pt particles at different stages of evaluation of ECS. Particle (a) is the furthest from reaching its equilibrium state, while particle (c) is the closest to the ECS.

4.4.1 Determining the ECS

The ECS of the Pt particles was determined using electron diffraction combined with TEM, and Wulffman simulations. The ECS was found to consistently contain {100}, {111}, {220} and {113} facets as can be seen in Figure 19. It is important to note that {100} facets were not detected from electron diffraction, while it is logical to assume the existence of these facets. Moreover, the simulated ECS had a good fit with the experimental HRSEM micrographs of the Pt particles, which reinforces the existence of {100} facets. Additional (smaller) facets with higher energy are also likely to be present, but these facets were not detected by TEM or HRSEM analysis. Facet surface energy ratios from the equilibrated particles, as measured for the particle in Figure 19, were $\gamma(Pt_{113})/\gamma(Pt_{111})=1.065$ and $\gamma(Pt_{220})/\gamma(Pt_{111})=1.07$. Based on Figure 19 it is not possible to determine the exact $\gamma(Pt_{100})/\gamma(Pt_{111})$ ratio, however, using Wulffman software simulations, this ratio was estimated to be greater than 1.08.

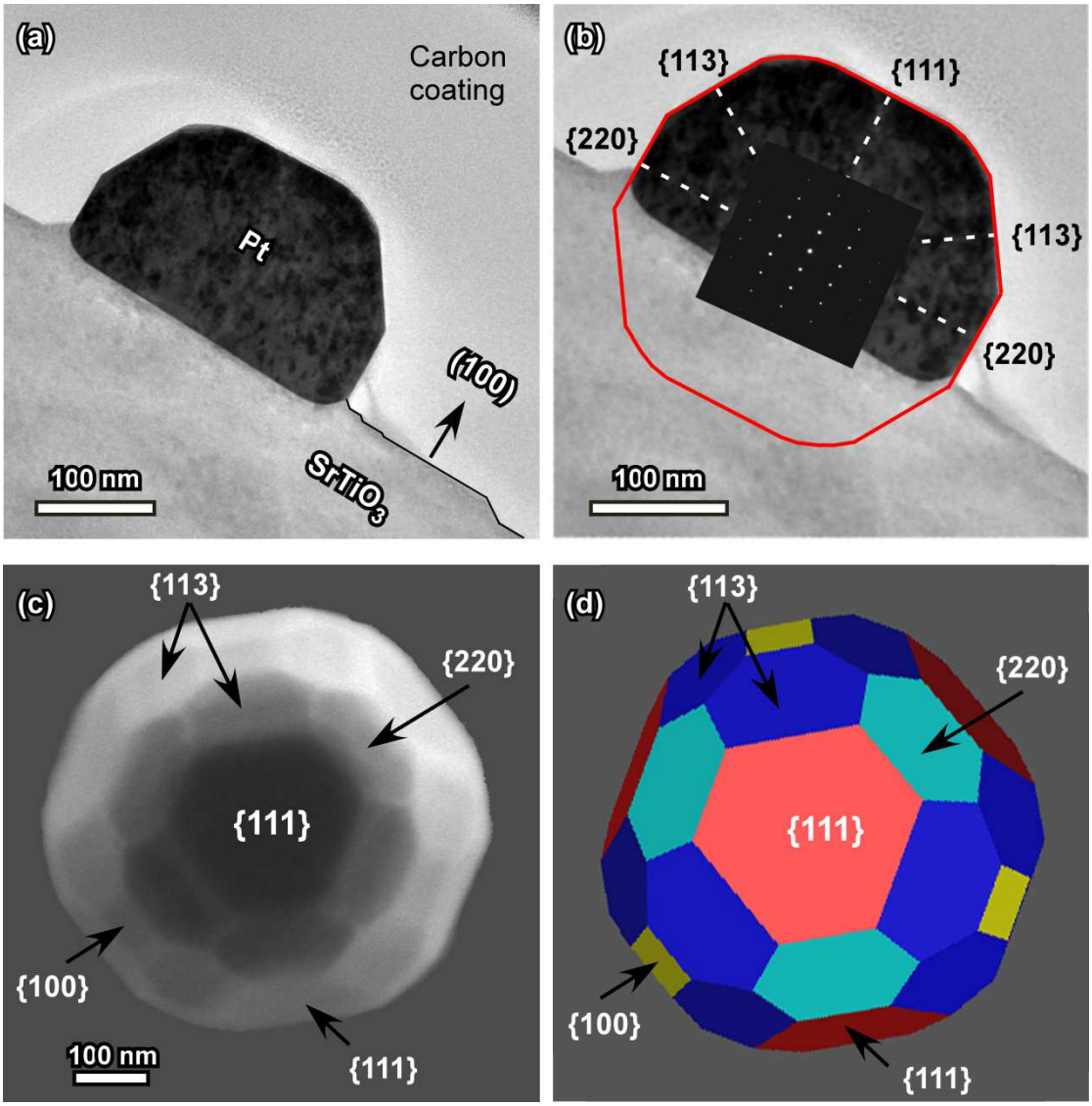

Figure 19: (a) Bright field TEM micrograph of a cross-section view of a Pt particle equilibrated on the $SrTiO_3$ substrate. (b) Partial solution of the ECS of the particle presented in (a). (c) HRSEM plan-view micrograph of a typical Pt particle. (d) Simulation of the ECS of the Pt particle presented in (c)

4.4.2 Chemical Analysis of Equilibrated Particles

The chemical composition of the equilibrated Pt particles was determined using EDS in STEM mode. Besides the clear Pt signal, the spectra exhibited small signals from Sr and Ti, barely detectable over the background noise (Figure 20). To evaluate the significance of the Sr and Ti signals, the detection limit for both elements in platinum

was calculated using Equation (10) and the experimentally measured background and calculated k-factors from the TIA software[78]. The detection limit for element A in B is given by:

$$C_{\lim(A)} = k_{AB} \frac{f(P)\sqrt{2}\sqrt{N_{BG(A)}}}{N_B} \qquad (10)$$

where: k_{AB} is the k-factor, f(p) is a confidence probability factor, $N_{BG(A)}$ is the background count of element A and N_B is the count of element B (without background).

Quantitative analysis showed that while the Ti and Sr concentrations in the Pt particles were slightly higher than their detection limits, the detected concentration of both elements was extremely low (below 0.3 wt.%). In addition, the analysis from different areas of the Pt particles resulted in varying Ti and Sr concentrations, without a correlation between Ti or Sr concentration with distance from the substrate. As such, the detected Ti and Sr signals emanating from the Pt particles can't be associated with either Ti or Sr in solution due to spurious signals resulting from the adjacent substrate.

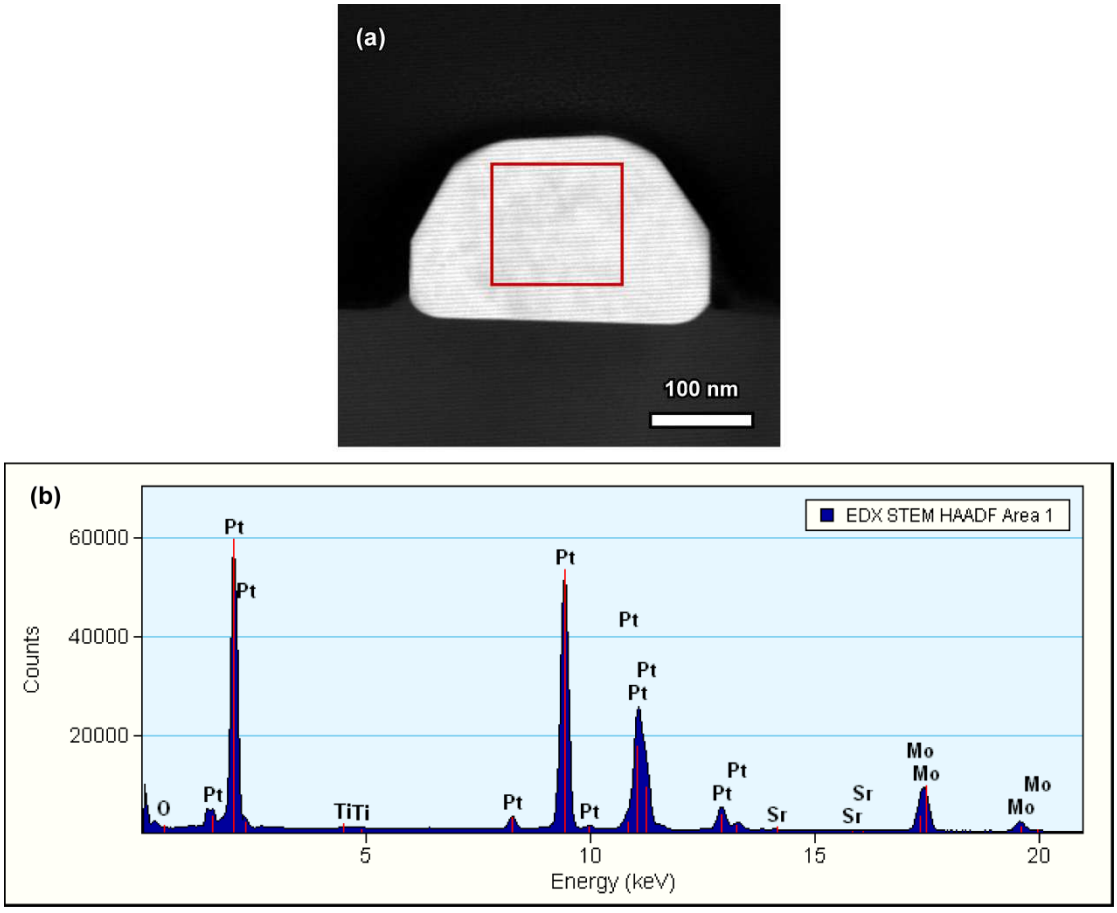

Figure 20: (a) HAADF STEM micrograph of selected particle. The red square marks the area where the EDS spectrum (b) was taken from.

4.5 Pt-$SrTiO_3$ Interfacial Energy

4.5.1 Particle-Substrate Misorientation

Figure 21 presents a TEM micrograph of a typical Pt particle on a (100)-$SrTiO_3$ substrate. Based on the electron diffraction pattern from the particle and the substrate, it can be seen that in this case the (111) planes of the particle are misoriented by ~1° relative to the (100) substrate planes. Larger misorientation angles were detected for other particles. In fact, all the examined particles exhibited some angular deviation of the (111) plane from the (100) substrate plane, ranging from ~1° to 6°. This evidence is also supported by the results achieved in the pole figure measurements. In the case

of the equilibrated particle presented in Figure 19(a), the misorientation is so large that it can be directly detected from the bright field TEM micrograph.

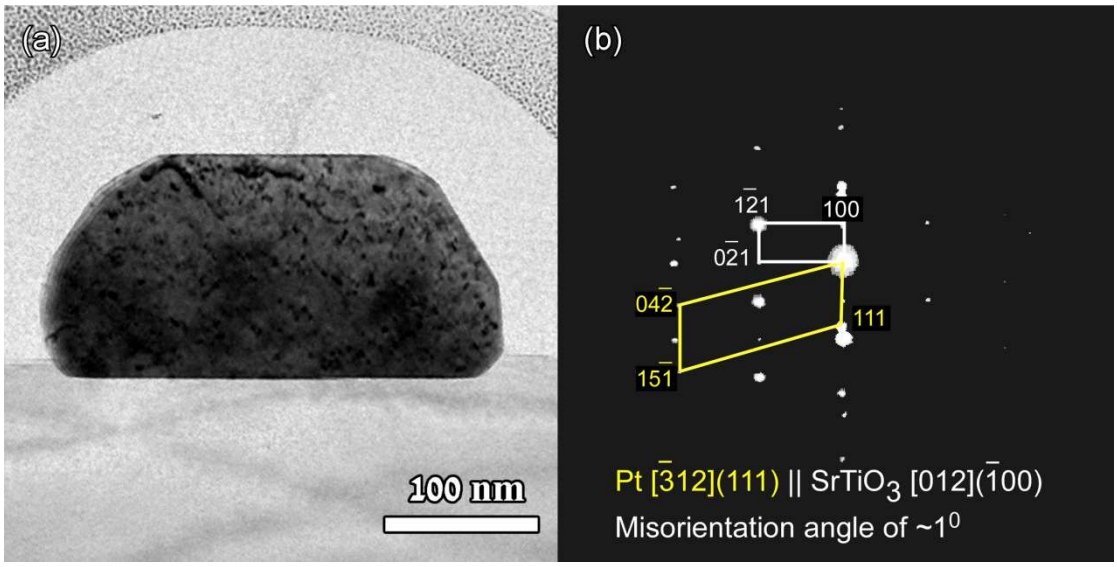

Figure 21: (a) Bright field diffraction contrast TEM micrograph of typical Pt particle equilibrated on a (100)-$SrTiO_3$ substrate (b) Electron diffraction from the particle and the substrate.

4.5.2 Determining the Interfacial Energy

For the particle shown in Figure 19(a) the substrate-particle interfacial energy was determined using the Winterbottom approach and ignoring the small ridges (less than 20 nm in height) seen in Figure 19, where the interface energy, $\gamma(Pt_{111}/STO_{100})$, can be determined from known values of the $SrTiO_3$ substrate ($\gamma(STO_{100})$) and particle ($\gamma(Pt_{111})$) surface energies, and from the measured relative distance from the particle Wulff point to the (111) facet and from the Wulff point to the interface (R_1/ R_2) [29]. R_1/ R_2 was measured from TEM micrographs to be 0.316, the $SrTiO_3$ (100) surface energy was taken from the literature to be 1.46 [J/m^2] [57], and the surface energy of the Pt (111) facet was taken to be1.95 [J/m^2] [79]. From equation *(9)*, the interface energy was determined to be $\gamma(Pt_{111}/STO_{100})$=2.08 J/m^2.

4.6 Atomistic Structure of the Interface

4.6.1 HRTEM Analysis of the Interface

To obtain better insight into the system, HRTEM and STEM analysis was conducted on the metal-oxide interfaces and adjacent free surfaces of the substrate. HRTEM can provide real space information at atomic resolution. However, due to specimen and microscope imperfections, interpretation of HRTEM data is not straightforward, and quantitative analysis is required to determine the local structure of the sample. Prior to conducting this analysis, the experimental micrographs were first Bragg-filtered to remove non-periodic signals, as demonstrated in Figure 22 [74].

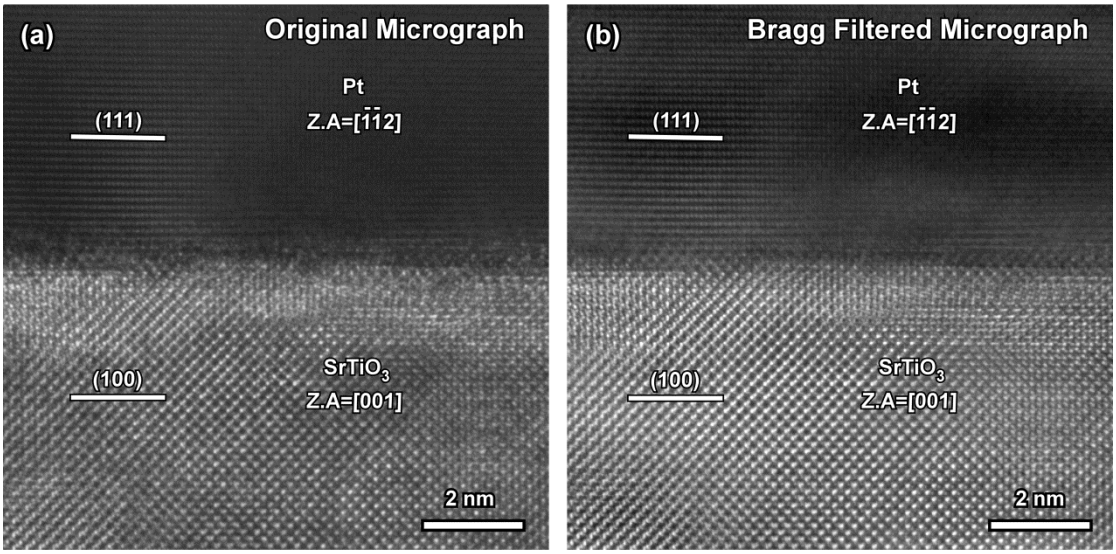

Figure 22:(a) An experimental HRTEM micrograph of the Pt/(100)-$SrTiO_3$ interface acquired at an objective lens defocus of -24 nm and a Cs of -7µm. (b) Bragg filtered image of the experimental micrograph presented in (a).

Analysis of the atomistic structure from the Bragg-filtered micrograph was conducted on the substrate area away from the interface (Figure 23). For the imaging conditions (objective lens defocus of -24 nm and Cs -7µm) and for this specific area of the sample (for this specific thickness) the bright dots in the micrograph coincide with Sr and Ti-O atomic columns. Moreover, it was possible to differentiate between these

columns due to their relative intensity, and to determine the exact position of atomic column type. Once the contrast of the HRTEM micrograph was associated with the atomic columns of the $SrTiO_3$ structure, it was possible to examine the interfacial area by periodically repeating the $SrTiO_3$ structure to the interface region (Figure 23). At the interface, the atom positions no longer coincide with the bright dots, due to changes in the thickness of the sample. In addition, the particle-substrate interface reveals 3-4 layers whose structure is neither that of ideal Pt, nor that of ideal $SrTiO_3$ (i.e. 3-4 layers atomic layers have reconstructed). However, due to changes in the thickness of the sample at the interface, and imperfections of the particular TEM sample, it was not possible to determine the exact atomistic structure at the interface.

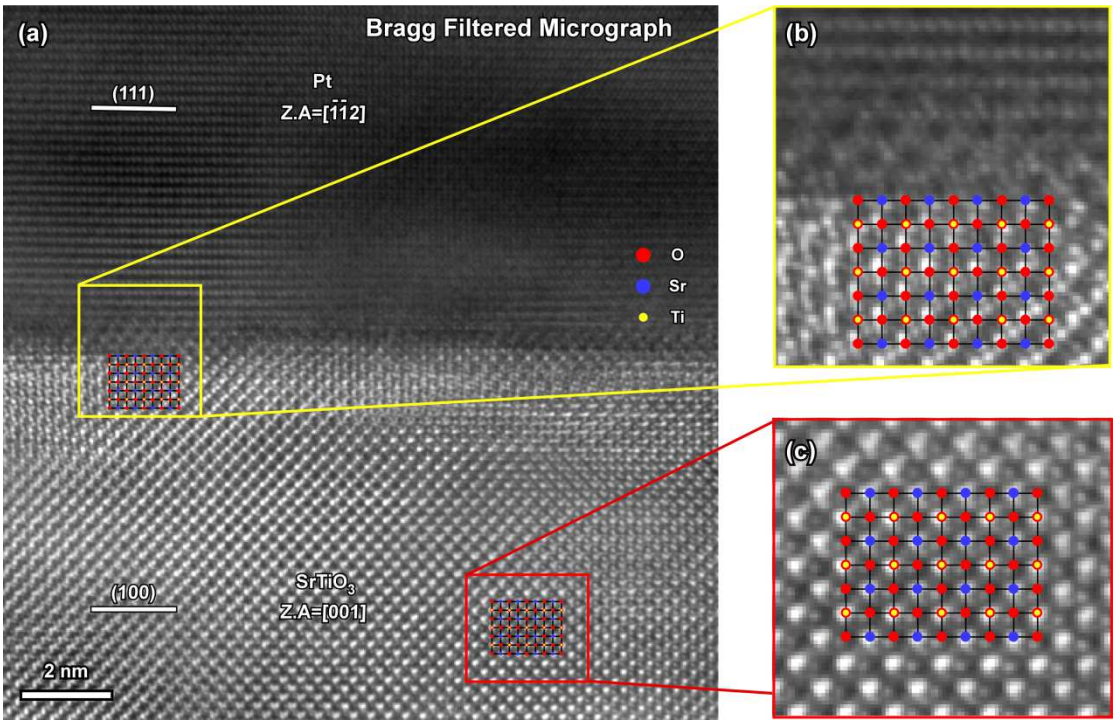

Figure 23: (a) HRTEM micrograph of the Pt-$SrTiO_3$ interface. (b) Atom positions in the $SrTiO_3$ at the region of (b) the interface, and (c) the bulk $SrTiO_3$.

4.6.2 HAADF STEM Analysis

HAADF STEM analysis was conducted on the substrate-particle interface and adjacent to the particle free surface of the substrate. HAADF STEM imaging is based

on mass-thickness contrast, [73]. As a result, for a constant thickness, it is possible to differentiate between different elements since elements with higher atomic number, will produce a stronger signal. HAADF STEM of the sample showed that the free surface termination of $SrTiO_3$, in the vicinity of the particles is SrO terminated (Figure 24), despite the chemical treatment of the substrate prior to Pt deposition, and subsequent dewetting, and whose purpose was to expose a uniform TiO_2 termination. Also, it was found from HAADF STEM (Figure 25) that the Pt particles are in direct contract with a substrate layer which has a mixed signal of Pt and Sr (or Ti) atoms over a distance of just over 1nm (Figure 25(c)), which also suggests that reconstruction took place at the interface.

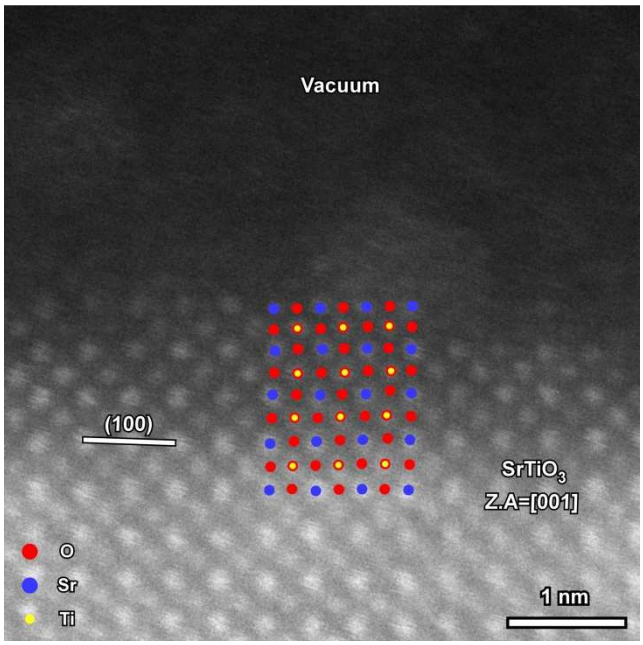

Figure 24: HAADF STEM micrograph of the free surface of $SrTiO_3$ adjacent to a Pt particle.

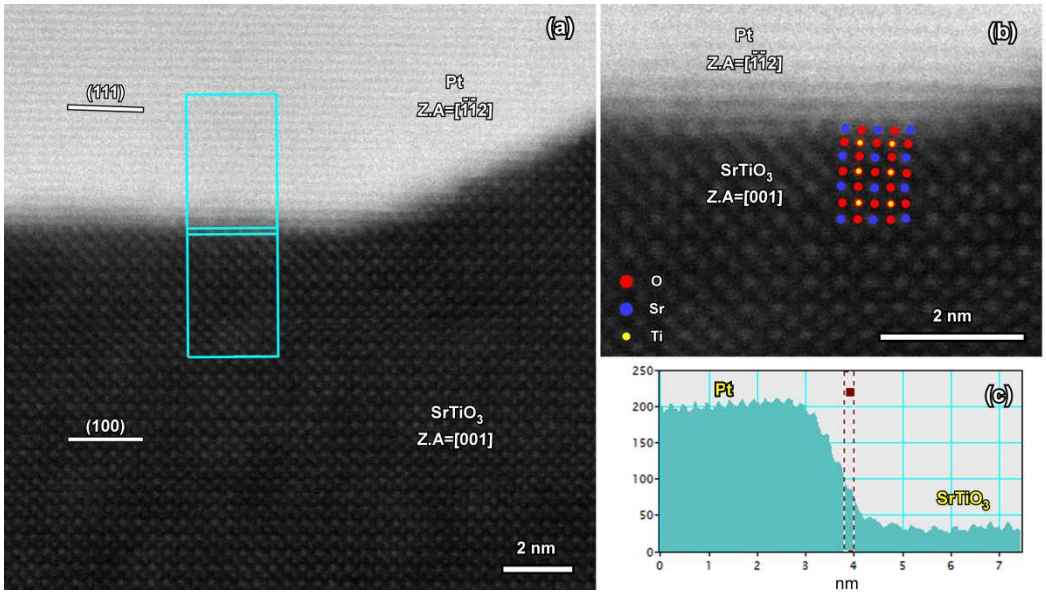

Figure 25:(a) HAADF STEM micrograph of a $SrTiO_3$-Pt interface. (b) Magnified view of the interfacial area. (c) Line-scan intensity profile of the area marked in (a), showing the decaying HAADF signal (from the Pt to the $SrTiO_3$) at the interface.

5. Discussion

5.1 ECS of Pt

5.1.1 Previous Works Conducted on ECS of Pt

The ECS of a single crystal particle is the most stable thermodynamic form of the particle, and is affected by several factors such as equilibration temperature, atmosphere, pressure, and solute activity [80]. In general, under constant pressure, with increasing annealing temperature, the ECS should become more isotropic, forming a perfect droplet above the melting temperature. This temperature dependent behavior was confirmed for Pt by Mclean et al. [81]. Furthermore, it was shown by Wang et al. that the Pt particle shape can be easily modified with exposure to different gases [82], as can be seen in Figure 26. Pt particles grown in N_2 were similar in size and distribution to Pt particles grown in H_2, however they had fundamental differences in shape. In addition, they reported that annealing Pt square particles, initially grown in the presence of H_2, in a N_2 transformed the Pt cubes to spheres, suggesting that the Pt ECS shape is very much environment dependent.

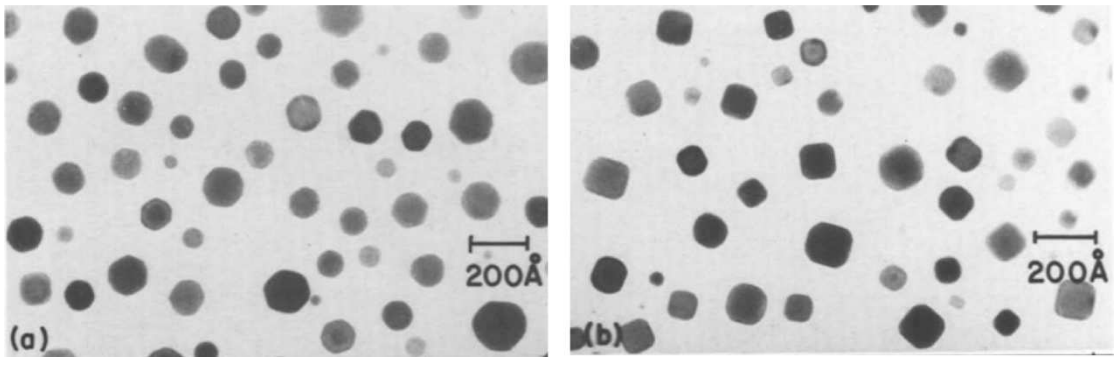

Figure 26: TEM micrographs of Pt particles on planar amorphous SiO_2: (a)Predominantly hexagonal particles are observed following growth in N_2 at 600°C, (b)while exclusively squares and rectangles are observed following growth in H_2 [82].

Lee et al. equilibrated Pt particles supported on a thin Pt foil in ultra-high vacuum at 1200°C and at a $P(O_2)$ of $1.32x10^{-10}$ atm, which after rapid cooling to room temperature resulted in a spherical shape with distinct {100} and {111} facets, separated by curved (i.e., stepped) regions [83].Similar experiments with carbon contamination produced cubo-octahedron shaped Pt particles with large {111}, {100}, and {110} facets delimited by curved surfaces. Iddir et al. also annealed Pt particles at 1150°C, but under nitrogen instead of vacuum and for a limited annealing time of 10 minutes, followed by slow cooling to room temperature [63]. The resulting particles exhibited an octahedral shape with mainly {111} and {100} facets in addition to the presence of small {110} facets.

Ramachandran et al. produced cubo-octahedron Pt particles with {111} and {100} facets meeting at sharp corners after annealing in H_2 at 650°C and in vacuum at 900°C [84]. However, annealing the same particles in air at 650°C produced round particles with {111}, {100} and {110} facets and no sharp corners. Other groups reported that annealing at lower temperatures (below 500°C) and at higher values of $P(O_2)$ resulted in rounding of the particles, as a result of oxygen adsorption, which probably indicates that steps and higher index facets were formed, while annealing Pt in a reducing atmosphere (hydrogen) led to cubo-octahedral particles with {100}, {111} facets and sometimes even small {110} facets [85,86].

In the present study, which included annealing at a relatively high $P(O_2)$ of $1.5x10^{-3}$ atm followed by slow cooling to room temperature, the ECS of Pt is a multi-faceted shape with rounded corners. The particles were annealed at a relatively high

temperature, which could explain the rounded form, had it not been for the post-annealing slow cooling rate which should decrease the isotropy.

5.1.2 Has the Particle Reached its ECS?

The surface and interfacial energies analysis were conducted on the particle presented in Figure 19. One of the interesting questions regarding this particle is whether it has reached its ECS, since the answer to this question has an impact of the extracted thermodynamic data.

On one hand, Pt particles in this system seem to equilibrate by the TLK model, as can be seen in Figure 18. The steps on some of the facets indicate that the particle shape is still in the formation progress. In the particle presented in Figure 19 and then again in Figure 27(a),(d), these steps are absent, which indicates that the relevant facets have reached their final state and that the particle itself has reached its ECS. However, since the top (111) facet of the particle doesn't exhibit a perfect hexagon, it indicates that the particle almost reached its ECS, and that the macro-scale steps of growth mechanism disappear prior to particle reaching its final ECS.

5.1.3 ECS of Supported Pt Particle Formed in High $P(O_2)$

Here, the ECS of Pt equilibrated in the presence of oxygen consists of at least 4 types of facets: {111}, {100}, {110} and {113}. As expected for a FCC metal, {111} facets were found to be dominant [87]. A less expected result was the limited size (area) of {100} facets (Figure 19). The experimentally obtained ratio of $\gamma_{hkl}/\gamma_{111}$ is compared to the reported (calculated) values from the literature in Table 2 [88,89,90,91]. As

predicted by theoretical calculations, the {100} surface energy is higher than that of {111}. In addition, {113} facets were detected in the ECS. The only other study which detected {113} facets was that conducted by Rupprechter et al. [85].

Table 2: Comparison of the experimentally determined Pt surface energy ratios to values from the literature.

$\gamma_{100}/\gamma_{111}$	$\gamma_{110}/\gamma_{111}$	$\gamma_{113}/\gamma_{111}$	**Calc/Exp**	**Reference**
> 1.08	1.07	1.065	Present Study	
1.19	1.23	-	Calculated	[87]
1.06	-	-	Calculated	[88]
1.24	1.39	-	Calculated	[89]
1.15	1.22	-	Calculated	[90]
1.38	1.45	1.43	Calculated	[91]

Using the obtained surface energies for {113} and {220} facets, the ECS of Pt was simulated using Wulffman software. The top and side view of the simulations can be seen in Figure 27 (b) and (e) respectively. As previously stated, the observed particle almost reached its equilibrium form. Using the same simulated software, the simulations of totally equilibrated particle were formed (Figure 27(c) and (f)). The analysis of the ECS of the Pt particle and crystal shape of the experimentally observed particle showed that there is about 1-2% of error in the measured values of the surface and interfacial energies. It is important to note that the experimental values were obtained from analysis of a single particle, due to the statistical limitations involved in TEM analysis, and therefore the actual error in the surface and interfacial energies is probably larger. Given the lack of statistical analysis in the present study, based on Table 2 it can be seen that experimental surface energies for Pt are significantly lower

than those predicted by simulations, emphasizing the importance of experimental analysis for this system.

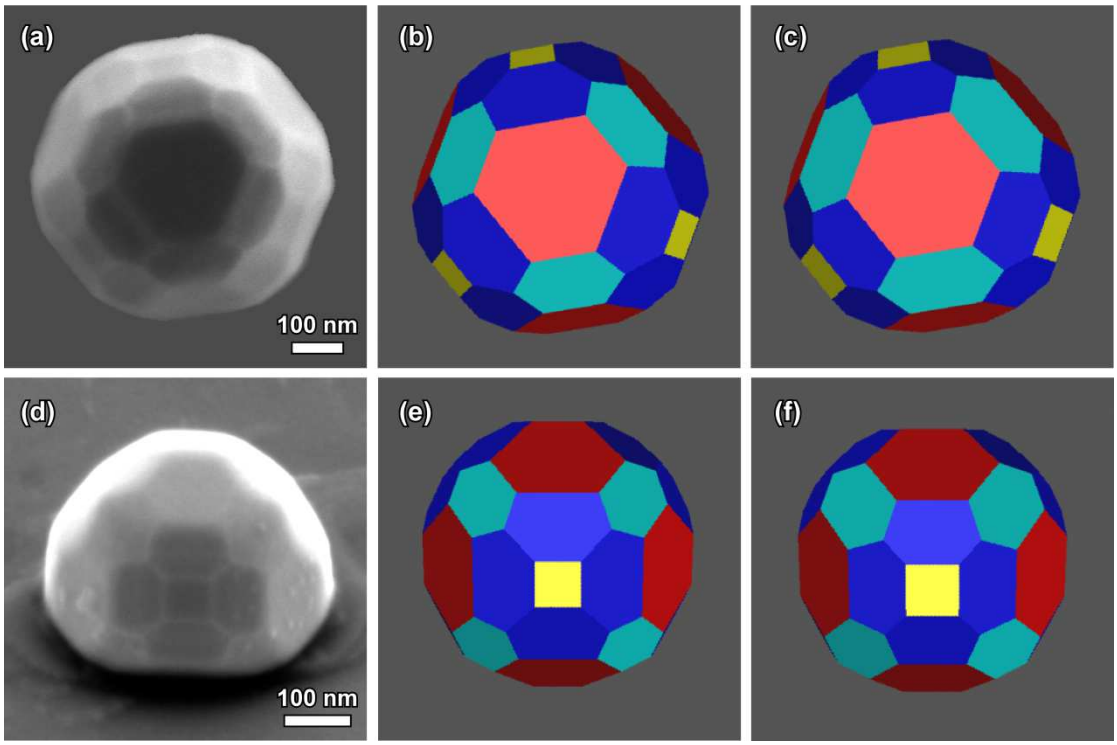

Figure 27: (a) and (d) Experimental micrographs showing plan and side views of the Pt particle, respectively. The Pt particle is the same one as in Figure 19. (b) and (e) Simulations of the ECS of the Pt particle (plan and side view) presented in (a), based on the extracted experimental data. (c) and (f) Simulations of the ECS of the Pt particle presented in (a), whether it had reached a total equilibrium state.

5.1.4 Chemical Analysis of Pt Equilibrated Particles

Chemical analysis of the equilibrated particles indicated that both elements, Ti and Sr, may be present in the Pt matrix, slightly above the detection limit, although their total concentration was extremely low. Since the Pt particle was attached to the $SrTiO_3$ substrate during EDS analysis, secondary effects such as fluorescence and multiple scattering may result in Ti and Sr signals detected from the Pt particle. While such secondary effects are normally minor in TEM analysis, and thus have a small contribution to the quantitative analysis, given the small overall signal detected here

secondary effects can't be neglected. In addition, there is a high probability that during sample preparation by FIB, some redeposition of elements occurred. This assumption is supported by the fact that the Ti and Sr signals were not constant within the Pt particle, and no correlation between the distance from the substrate and the Sr/Ti signals was found. This implies that one cannot conclude that the Pt particles contained Ti and Sr in solution, and therefore we assume that they did not influence the ECS of Pt, and the rounded particle shape indeed reflects the ECS of Pt equilibrated in the presence of oxygen.

5.2 The Interfacial Energy between the Pt and $SrTiO_3$

The interfacial energy between the Pt particle and $SrTiO_3$ was determined to be 2.08 J/m^2. To determine this value, R_1 and R_2 were measured for the particle in Figure 19, as required for Winterbottom analysis [29]. As stated above, for an unknown reason, each particle exhibited some inclination relative to the substrate. Since there is a variety in the degree of particle inclination, each particle has a slightly different R_1/R_2 ratio (Figure 28), which necessarily means a different interfacial energy for each particle. However, since the particles have a distribution of in-plane orientations, due to the lack of a low-index orientation relationship with the substrate, it is possible to assume that the interfacial energy is similar for each particle and that 2.08 J/m^2 represents the average interfacial energy for the observed preferred orientation. To the best of the authors' knowledge, this is the only experimentally determined value of interface energy between Pt and undoped (100) $SrTiO_3$.

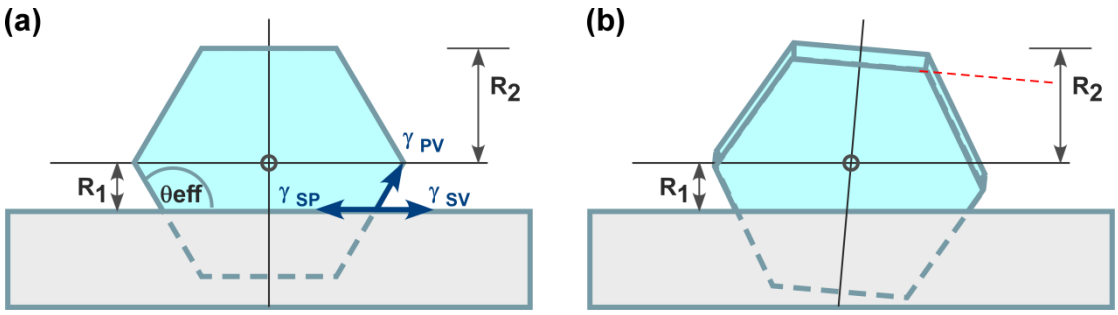

Figure 28: Schematic drawing showing the source of error in determining the interface energy due to inclination of an equilibrated Pt particle on the $SrTiO_3$ substrate

The experimentally determined value of the Pt-$SrTiO_3$ interfacial energy (2.08 J/m^2) is relatively high, which may suggest that this coupling is not very favorable, and there is poor adhesion between $SrTiO_3$ and Pt. However, one should remember that the ECS of a particle supported on a substrate is the product of equilibrium between three phases, and all the surface and interfacial energies contribute to the degree of particle wetting on the substrate. Also, one should take into consideration that the interfacial energy was determined using theoretically calculated values for $SrTiO_3$ (100) and Pt (111). There is a large variation of calculated values in the literature, especially for $SrTiO_3$ (100).

5.3 Substrate Morphology

The dewetting process used to form equilibrated particles had an effect not only on the Pt film, but also on the substrate. Following annealing, the substrate's morphology changed from atomically flat steps, to a surface composed of terraces. Many of the Pt particles were found on top of pedestals formed of dense $SrTiO_3$ steps. This configuration is unusual, since it necessarily means an increased area of the substrate adjacent to the equilibrated particle.

These results can be explained by the combination of two processes which occur during the dewetting process; substrate evaporation and film retraction. As long as the substrate was covered by the Pt film, it was protected from evaporation. As the film gradually agglomerated, new areas of the substrate were exposed, and evaporation of the exposed $SrTiO_3$ occurred, creating a non-uniform morphology of the surface (roughness). In Figure 15(a), the retraction path of the film can be clearly seen, leaving behind a rough pattern in the substrate. Evaporation can also explain the presence of steps beneath the particles. During annealing, the Pt prevents evaporation. As a result, the particle locations act as accumulation sites for step bunching.

5.4 Pt and (100)-$SrTiO_3$ Orientation Relationship

The crystalline properties of a supported single crystal metal particle are determined by factors such as mismatch in the lattice parameter with the supporting substrate, substrate surface morphology, deposition method and annealing treatment. However, if the crystal has reached thermodynamic equilibrium, then the method of deposition becomes irrelevant.

Cubic Pt and (100)-$SrTiO_3$ have very similar lattice parameters, yet the experimental results showed that at equilibrium a cube on cube orientation relationship does not exist. Detailed analysis showed that in most cases the Pt(111) planes were parallel to the (100)-$SrTiO_3$ substrate. In addition, the Pt particles exhibited no definite low-index preferred in-plane orientation relationship with the substrate. This suggests that a small lattice misfit between the metal and the oxide substrate is not a sufficient condition to form highly oriented particles.

Annealing can play an important role on the particle properties. Temperature, pressure, annealing atmosphere and contaminants all contribute not only to the particle ECS but also to the particle orientation with regards to the substrate. According to the literature, achieving a {100}-Pt orientation requires higher annealing temperatures [58,59]. Also, it was noted that annealing Pt in the presence of oxygen in the gas mixture contributes to elimination of surface impurities which serve as nucleation sites for {111}-Pt texture, and as a result supports Pt{100}-orientation formation [59,60,61,62]. In the present study the samples were annealed at 1050°C in Ar/2%O_2, but a low-index orientation relationship was not formed. This indicates that the substrate surface structure may play a significant role in determining particle-substrate orientation relationships.

$SrTiO_3$ can be visualized as constructed of alternating layers of SrO and TiO_2. It was reported that the interface energy with Pt depends on the (100) termination of $SrTiO_3$ (SrO or TiO_2), which in turn affects the equilibrium Pt orientation with (100)-$SrTiO_3$ [63,64]. Following the premise that the nature of the surface termination can be controlled by sample preparation methods [66,67,68], the substrates used in this study were treated prior to Pt deposition to create TiO_2-terminated $SrTiO_3$, which according to the literature should favor highly oriented particles. However, {111}-oriented particles were formed without a low-index orientation relationship. In addition, HRTEM analysis combined with HRSTEM analysis showed that at the Pt-$SrTiO_3$ interface, the $SrTiO_3$ is probably terminated with a SrO layer, followed by a reconstructed surface, whose structure is unknown. Moreover, HAADF STEM analysis of the free surface adjacent to the particle showed that the $SrTiO_3$ is SrO-

terminated, despite the substrate treatment procedure. This also indicates that evaporation of $SrTiO_3$ probably occurred, and implies that in the given experimental conditions, SrO termination is more stable.

(100)-$SrTiO_3$ is known to be sensitive to its environment and was reported to easily undergo surface reconstruction, even with minor changes in temperature and $P(O_2)$. The most commonly reported surface reconstructions for $SrTiO_3$ are (2x1) [8,92], c(4x2) [8,92,93] and c(6x2) [8,93], while other forms of reconstructions were also reported [92,94,95]. In the present study, the structure of the reconstructed surface was not determined, however the evidence strongly suggests that $SrTiO_3$ reconstruction took place during equilibration. This reconstruction is actually a complexion, and it results in a high-index orientation relationship instead of a cube on cube orientation relationship [2].

5.5 Experimental Limitations

In the present work, some thermodynamic data was extracted for Pt particles equilibrated in high $P(O_2)$. Much of the analyses was conducted on a single Pt particle. A single particle, of course, provides poor statistics. This is due to some reservations and technical limitations that were encountered during this research work and should be mentioned.

The first issue was that for these analyses FIB samples were required. The preparation of each FIB sample requires many hours of meticulous labor. Each sample contained only one particle of interest, and while more than one sample was prepared, only a few of them were sufficient in quality for subsequent electron microscopy.

An additional handicap was the small size of the equilibrated Pt particles. Particles that were close to equilibrium were easy to detect by SEM. However, only after TEM sample preparation was it possible to determine if an individual particle had reached equilibrium. Many of the prepared FIB samples contained particles that were not equilibrated. In addition, for surface and energies analyses, cross section of the exact middle of the particle was required. This task was compounded by the small dimensions of the equilibrated particles.

Another issue was due to the lack of low-index orientation relationship between the particles and the substrate. FIB samples that were prepared for substrate atomistic analysis couldn't be used for Winterbottom's analysis. Since the particles were misoriented and inclined regarding the substrate, the cross section of these particles often truncated their shape, which made it impossible to detect the Wulff point, required for Winterbottom's analysis. Therefore, special FIB samples were required to be made for the Winterbottom's analysis. In these cases, the particle was aligned, but the substrate was misoriented, and couldn't be used for atomistic analysis.

6. Summary and Conclusions

In the present study, Pt thin films were equilibrated on chemically treated single crystal (100)-$SrTiO_3$ substrates in the solid-state and in the presence of an Ar/2%O_2 carrier gas. Following the dewetting process, single crystal Pt particles were formed, although only the smaller particles reached their ECS after 10 hours of the annealing treatment. Also, after dewetting, the substrates exhibited a certain degree of roughness, which implied that some evaporation of $SrTiO_3$ took place along with the retraction of the Pt film.

Despite the very similar lattice parameters of Pt and (100)-$SrTiO_3$, a cube-on cube orientation relationship was not formed. Moreover, the Pt particles with a {111} preferred orientation to the (100)-$SrTiO_3$ had no low index in-plane preferred orientation relationship. Atomistic analysis of the interface suggested that $SrTiO_3$ reconstruction took place during equilibration. This resulted in a preferred orientation instead of a cube-on-cube low-index orientation relationship.

The equilibrium crystal shape of the Pt particles was found to include the following facets: {111}, {100}, {110} and {113}, although, additional facets may be present as well. The relative surface energies were found to be $\gamma(Pt_{113})/\gamma(Pt_{111})=1.065$ and $\gamma(Pt_{220})/\gamma(Pt_{111})=1.07$, with a possible error of at least 2%. The particle-substrate solid-solid interfacial energy was determined to be $\gamma(Pt_{111}/STO_{100})=2.08$ J/m^2.

7. Recommendations for Future Work

- TEM in-situ heating of the Pt film supported on $SrTiO_3$ will help to further understand the morphological evolution of both the particles and the substrate during annealing. HRTEM has the potential to track the atomic changes at the interface, including a change of the substrate termination. Also, in situ SEM experiments will help to understand the kinetics by which Pt particles reach their equilibrium state. The only problematic challenge for in-situ experiment is the set value of oxygen partial pressure for the systems available at the Technion. Environmental TEM holders and SEMs may offer more flexibility in oxygen partial pressure, but these systems always have poorer resolution.
- The termination of (100) $SrTiO_3$ should be characterized as a function of annealing conditions (oxygen partial pressure and temperature).
- In the current work, the major facets of the ECS of the Pt were determined. However, there is a high probability that additional facets, with higher energies, are also present in the shape. The remaining facets belonging to the ECS of Pt equilibrated at high $P(O_2)$ should be characterized. This can be done by making additional FIB samples, each one from a different direction of the Pt crystal.
- It is recommended to do additional surface and interface energies measurements (for new equilibrated particles) in order to acquire a better statistics.
- Additional methods should be employed to confirm the lack of Sr and Ti in solution in the Pt particles. Atom probe tomography may be a viable experimental approach.
- The main goal of the future work will be determination of the surface reconstruction of $SrTiO_3$ as a function of equilibration conditions, such that Pt-

$SrTiO_3$ adopts the reported cube-on-cube orientation relationship. This can be done by in-situ TEM heating combined with extensive TEM work at the interface from at least two different directions.

8. References

1 A. Marmur, *Solid-surface characterization by wetting*, **39**:473-489, 2009.

2 W. D. Kaplan, D. Chatain, P. Wynblatt, W. C. Carter, *A review of wetting versus adsorption, complexions, and related phenomena: The rosetta stone of wetting*, Journal of Materials Science, **48**[17]:5681-5717, 2013.

3 T. Young, *An Essay on the Cohesion of Fluids*, Philosophical Transactions of the Royal Society of London, **95**:65-87, 1805.

4 E. Saiz, A. P. Tomsia, R. M. Cannon, *Ridging effects on wetting and spreading of liquids on solids*, ActaMaterialia, **46**[7]:2349-2361, 1998.

5 G. Levi, W. D. Kaplan, *Aluminium-alumina interface morphology and thermodynamics from dewetting experiments*, ActaMaterialia, **51**[10]:2793-2802, 2003.

6 M. Cherkaoui, L. Capolungo. Atomistic and Continuum Modeling of Nanocrystalline Materials: Deformation Mechanisms and Scale Transition. New York: Springer, 2009.

7 J. M. Howe. Interfaces in Materials: Atomic Structure, Thermodynamics and Kinetics of Solid-Vapor, Solid-Liquid and Solid-Solid Interfaces. New York: John Wiley & Sons, 1997.

8 N. Erdman, L. D. Marks, *$SrTiO_3$(001) surface structures under oxidizing conditions*, Surface Science, **526**[1]:107-114, 2003.

9 T. Imayoshi, H. Oigawa, H. Shigekawa, H. Tokumoto, *Surface reconstruction of GaAs(001) nitrided under the controlled As partial pressure*, Surface Science, **540**[1]:L577-L582, 2003.

10 I. Kamiya, D. E. Aspnes, H. Tanaka, L. T. Florez, J. P. Harbison, R. Bhat, *Surface science at atmospheric pressure: Reconstructions on (001) GaAs in organometallic chemical vapor deposition*, Physical Review Letters, **68**[5]:627-630, 1992.

11 H. J. Gao, Y. L. Wang, H. M. Guo, Z. H. Qin, H. F. Ma, *Toward a detailed understanding of Si(111)- 7×7 surface and adsorbed ge nanostructures: Fabrications, structures, and calculations*, Journal of Nanomaterials, **2008**[1]:2008.

12 N. P. Guisinger, S. P. Elder, N. L. Yoder, M. C. Hersam, *Ultra-high vacuum scanning tunnelling microscopy investigation of free radical adsorption to the Si(111)-7 × 7 surface*, Nanotechnology, **18**[4]:2007.

13 M. Chida, Y. Tanishiro, H. Minoda, K. Yagi, *Growth mechanism of 7×7 domains from the `1×1' phase on a quenched Si(111) surface studied by high temperature STM*, Surface Science, **423**[1]:L236-L243, 1999.

14 H. Meltzman, D. Mordehai, W. D. Kaplan, *Solid–solid interface reconstruction at equilibrated Ni–Al2O$_3$ interfaces*, ActaMaterialia, **60**[11]:4359-4369, 2012.

15 D. Chatain, P. Wynblatt, G. S. Rohrer, *Equilibrium crystal shape of Bi-saturated Cu crystals at 1223 K*, ActaMaterialia, **53**[15]:4057-4064, 2005.

16 H. Sadan, W. Kaplan, *Au–Sapphire (0001) solid–solid interfacial energy*, Journal of Materials Science, **41**[16]:5099-5107, 2006.

17 C. V. Thompson, *Solid-State Dewetting of Thin Films*, Annual Review of Materials Research, **42**:399-434, 2012.

18 D. Srolovitz, S. Safran, *Capillary instabilities in thin films. I. Energetics*, Journal of Applied Physics, **60**[1]:247-254, 1986.

19 W. Kossel, *Extenoling the Law of Bravais*, NachGesWiss Gottingen, 143, 1927.

20 I. N. Stranski, *ZurTheorie des Kristallwachstums*, Z. Phys. Chem, **136**:259-278, 1928.

21 H. P. Bonzel, *3D equilibrium crystal shapes in the new light of STM and AFM*, Physics Reports, **385**[1–2]:1-67, 2003.

22 J. B. Hudson. Surface Science: An Introduction. New York: John Wiley & Sons, 1992.

23 L. Xiang-Yang, P. Bennema, J. P. van der Eerden, *Rough-Flat-Rough Transition of Crystal Surfaces*, Nature, **356**[6372]:778, 1992

24 W. L. Winterbottom, N. A. Gjostein, *Determination of the anisotropy of surface energy of metals—I: Theoretical analysis*, ActaMetallurgica, **14**[9]:1033-1040, 1966.

25 G. Wulff, *ZurFrageDerGeschwindigkeit DesWachstums Und Der Auflosung Der Krystalflachen*, Z. Krystallogr. Mineral, **34**:449-530, 1901.

26 C. L. Johnson, E. Snoeck, M. Ezcurdia, B. Rodriguez-Gonzalez, I. Pastoriza-Santos, L. M. Liz-Marzan, M. J. Hytch, *Effects of elastic anisotropy on strain distributions in decahedral gold nanoparticles*, Nat Mater, **7**[2]:120-124, 2008.

27 A. S. Masadeh, E. S. Božin, C. L. Farrow, G. Paglia, P. Juhas, S. J. L. Billinge, A. Karkamkar, M. G. Kanatzidis, *Quantitative size-dependent structure and strain determination of CdSe nanoparticles using atomic pair distribution function analysis*, Physical Review B, **76**[11]:115413, 2007.

28 H. Meltzman, D. Chatain, D. Avizemer, T. M. Besmann, W. D. Kaplan, *The equilibrium crystal shape of nickel*, ActaMaterialia, **59**[9]:3473-3483, 2011.

29 W. L. Winterbottom, *Equilibrium shape of a small particle in contact with a foreign substrate*, ActaMetallurgica, **15**[2]:303-310, 1967.

30 K. Yasuda, T. Masui, T. Miyamoto, N. Imanaka, *Catalytic combustion of methane over Pt and PdO-supported CeO2–ZrO2–Bi2O3/γ-Al2O3 catalysts*, Journal of Materials Science, **46**[11]:4046-4052, 2011.

31 A. Topalidis, D. E. Petrakis, A. Ladavos, L. Loukatzikou, P. J. Pomonis, *A kinetic study of methane and carbon dioxide interconversion over 0.5%Pt/$SrTiO_3$ catalysts*, Catalysis Today, **127**[1-4]:238-245, 2007.

32 H. Liu, C. Song, L. Zhang, J. Zhang, H. Wang, D. P. Wilkinson, *A review of anode catalysis in the direct methanol fuel cell*, Journal of Power Sources, **155**[2]:95-110, 2006.

33 X. Jiang, H. Huang, F. B. Prinz, S. F. Bent, *Application of Atomic Layer Deposition of Platinum to Solid Oxide Fuel Cells*, Chemistry of Materials, **20**[12]:3897-3905, 2008.

34 H. Yoshida, Y. Yazawa, T. Hattori, *Effects of support and additive on oxidation state and activity of Pt catalyst in propane combustion*, Catalysis Today, **87**[1–4]:19-28, 2003.

35 H. Meixner, U. Lampe, *Metal oxide sensors*, Sensors and Actuators B: Chemical, **33**[1–3]:198-202, 1996.

36 H. Meixner, J. Gerblinger, U. Lampe, M. Fleischer, *Thin-film gas sensors based on semiconducting metal oxides*, Sensors and Actuators B: Chemical, **23**[2-3]:119-125, 1995.

37 P. D. Hren, S. H. Rou, H. N. Al-Shareef, M. S. Ameen, O. Auciello, A. I. Kingon, *Bottom electrodes for integrated Pb(Zr, Ti)O_3 films*, Integrated Ferroelectrics, **2**[1-4]:311-325, 1992.

38 O. Moran, R. Hott, R. Schneider, J. Halbritter, *Transport properties of ultrathin $SrTiO_3$ barriers for high-temperature superconductor electronics applications*, Journal of Applied Physics, **94**[10]:6717-6723, 2003.

39 J. Rodriguez Contreras, H. Kohlstedt, U. Poppe, R. Waser, C. Buchal, N. A. Pertsev, *Resistive switching in metal-ferroelectric-metal junctions*, Applied Physics Letters, **83**[22]:4595-4597, 2003.

40. V. Mikhelashvili, Y. Shneider, B. Meyler, G. Atiya, S. Yofis, T. Cohen-Hyams, W. D. Kaplan, M. Lisiansky, Y. Roizin, J. Salzman, G. Eisenstein, *Non-volatile memory transistor based on Ptnanocrystals with negative differencial resistance*, Journal of Applied Physics, **112**[2]:024319-5, 2012.

41. V. Mikhelashvili, B. Meyler, Y. Shneider, S. Yofis, J. Salzman, G. Atiya, T. Cohen-Hyams, G. Ankonina, W. D. Kaplan, M. Lisiansky, Y. Roizin, G. Eisenstein, *Ultraviolet to near infrared response of optically sensitive nonvolatile memories based on platinum nano-particles and high-k dielectrics*

on a silicon on insulator substrate, Journal of Applied Physics, **113**[7]:074503-6, 2013.

42 Y. C. Liang, *Effect of conductive oxide buffering on structural and nanoscale electrical properties of ultrathin $SrTiO_3$ films on Pt electrodes*, Journal of Crystal Growth, **312**[9]:1610-1616, 2010.

43 D. Kan, K. Ito, Y. Shimakawa, *Local conduction in junctions composed of Pt and single-crystalline Nb-doped $SrTiO_3$*, Thin Solid Films, **518**[12]:3246-3249, 2010.

44 S.-S. Cho, H.-G.Kim, *Pt deposition effect for the catalyst of the semiconducting oxygen sensor*, IEEE International Symposium on Applications of Ferroelectrics, **2**:983-986, 1996.

45 X. B. Yan, K. Li, J. Yin, Y. D. Xia, H. X. Guo, L. Chen, Z. G. Liu, *The resistive switching mechanism of Ag/$SrTiO_3$/Pt memory cells*, Electrochemical and Solid-State Letters, **13**[3]:H87-H89, 2010.

46 H. Sim, D. J. Seong, M. Chang, H. Hwang, *Excellent resistance switching characteristics of Pt/single-crystal Nb-doped SrTiO3 Schottky junction*, 21st IEEE Non-Volatile Semiconductor Memory Workshop 2006, NVSMW 2006, **2006**:88-89, 2006.

47 G. Panomsuwan, O. Takai, N. Saito, *Optical and mechanical properties of transparent $SrTiO_3$ thin films deposited by ECR ion beam sputter deposition*, Physica Status Solidi (A) Applications and Materials Science, **210**[2]:311-319, 2013.

48 Y. Yamada, Y. Kanemitsu, *Band-to-band photoluminescence in $SrTiO_3$*, Physical Review B - Condensed Matter and Materials Physics, **82**[12]:2010.

49 M. Savinov, V. A. Trepakov, P. P. Syrnikov, V. Železný, J. Pokorný, A. Dejneka, L. Jastrabík, P. Galinetto, *Dielectric properties of Mn doped $SrTiO_3$*, Journal of Physics Condensed Matter, **20**[9]:2008.

50 P. Moetakef, J. R. Williams, D. G. Ouellette, A. P. Kajdos, D. Goldhaber-Gordon, S. J. Allen, S. Stemmer, *Carrier-controlled ferromagnetism in $SrTiO_3$*, Physical Review X, **2**[2]:2012.

51 R. M. Fernandes, J. T. Haraldsen, P. Wölfle, A. V. Balatsky, *Two-band superconductivity in doped $SrTiO_3$ films and interfaces*, Physical Review B - Condensed Matter and Materials Physics, **87**[1]:2013.

52 A. Barbier, C. Mocuta, D. Stanescu, P. Jegou, N. Jedrecy, H. Magnan, *Surface composition of $BaTiO_3/SrTiO_3(001)$ films grown by atomic oxygen plasma assisted molecular beam epitaxy*, Journal of Applied Physics, **112**[11]:2012.

53 Y. Tang, Y. Zhu, Y. Zhang, Z. Zhang, X. Ma, *Nanostructured $Nd_{0.45}Sr_{0.55}MnO_3$ films grown on $SrTiO_3(110)$*, Journal of Materials Research, **28**[13]:1692-1698, 2013.

54 D. R. Lide (Editor-in-Chief). Handbook of Chemistry and Physics, 87th Edition. Boca Raton: CRC Press, 2006-2007.

55 E. Heifets, E. A. Kotomin, J. Maier, *Semi-empirical simulations of surface relaxation for perovskite titanates*, Surface Science, **462**[1–3]:19-35, 2000.

56 J. Padilla, D. Vanderbilt, *Ab initio study of $SrTiO_3$ surfaces*, Surface Science, **418**[1]:64-70, 1998.

57 K. Johnston, M. R. Castell, A. T. Paxton, M. W. Finnis, *$SrTiO_3(001)(2\times1)$ reconstructions: First-principles calculations of surface energy and atomic structure compared with scanning tunneling microscopy images*, Physical Review B - Condensed Matter and Materials Physics, **70**[8]:085415-1-085415-12, 2004.

58 A. J. Francis, P. A. Salvador, *Crystal orientation and surface morphology of face-centered-cubic metal thin films deposited upon single-crystal ceramic substrates using pulsed laser deposition*, Journal of Materials Research, **22**[01]:89-102, 2007.

59 J. Son, J. Cagnon, S. Stemmer, *Strain relaxation in epitaxial Pt films on (001) $SrTiO_3$*, Journal of Applied Physics, **106**[4]:043525, 2009.

60 X. Chen, T. Garrent, S. W. Liu, Y. Lin, Q. Y. Zhang, C. Dong, C. L. Chen, *Scanning tunnelling microscopy studies of growth morphology in highly epitaxial c-axis oriented Pt thin film on (001) $SrTiO_3$*, Surface Science, **542**[3]:L655-L661, 2003.

61 X. M. Xu, J. Liu, Z. Yuan, J. Weaver, C. L. Chen, Y. R. Li, H. Gao, N. Shi, *Single crystalline highly epitaxial Pt thin films on (001) $SrTiO_3$*, Applied Physics Letters, **92**[10]:102102-102102-3, 2008.

62 T. Goto, J. R. Vargas, T. Hirai, *Effect of oxygen gas addition on preparation of iridium and platinum films by metal-organic chemical vapor deposition*, Materials Transactions, JIM, **40**[3]:209-213, 1999.

63 H. Iddir, V. Komanicky, S. Öğüt, H. You, P. Zapol, *Shape of Platinum Nanoparticles Supported on $SrTiO_3$: Experiment and Theory*, The Journal of Physical Chemistry C, **111**[40]:14782-14789, 2007.

64 A. Asthagiri, D. S. Sholl, *First principles study of Pt adhesion and growth on SrO- and TiO_2-terminated $SrTiO_3$(100)*, The Journal of Chemical Physics, **116**[22]:9914-9925, 2002.

65 A. D. Polli, T. Wagner, T. Gemming, M. Rühle, *Growth of platinum on TiO_2- and SrO-terminated $SrTiO_3$(100)*, Surface Science, **448**[2–3]:279-289, 2000.

66 K. Kawasaki M Fau - Takahashi, T. Takahashi K Fau - Maeda, R. Maeda T Fau - Tsuchiya, M. Tsuchiya R Fau - Shinohara, O. Shinohara M Fau - Ishiyama, T. Ishiyama O Fau - Yonezawa, M. Yonezawa T Fau - Yoshimoto, H. Yoshimoto M Fau - Koinuma, H. Koinuma, *Atomic Control of the $SrTiO_3$ Crystal Surface*, Science, **266**[5190]:1540-1542, 1994.

67 M. Kawasaki, A. Ohtomo, T. Arakane, K. Takahashi, M. Yoshimoto, H. Koinuma, *Atomic control of $SrTiO_3$ surface for perfect epitaxy of perovskite oxides*, Applied Surface Science, **107**[0]:102-106, 1996.

68 G. Koster, G. Rijnders, D. H. A. Blank, H. Rogalla, *Surface morphology determined by (001) singel-crystal $SrTiO_3$ termination*, Physica C: Superconductivity, **339**:215-230, 2000.

69 G. Atiya, V. Mikhelashvili, G. Eisenstein, W. D. Kaplan, *Solid-State Dewetting of Pt on (100) $SrTiO_3$*, submitted to the Journal of Materials Science, September 2013.

70 P. Thangadurai, Y. Lumelsky, M. S. Silverstein, W. D. Kaplan, *TEM specimen preparation of semiconductor–PMMA–metal interfaces*, Materials Characterization, **59**[11]:1623-1629, 2008.

71 M. Baram, W. D. Kaplan, *Quantitative HRTEM analysis of FIB prepared specimens*, Journal of Microscopy, **232**[3]:395-405, 2008.

72 P. Stadelmann, *EMS - a software package for electron diffraction analysis and HREM image simulation in materials science*, Ultramicroscopy, **21**[2]:131-145, 1987.

73 D. B. Williams, C. B. Carter. Transmission Electron Microscopy. New York: Springer, 2009.

74 Y. Kauffmann, A. Rečnik, W. D. Kaplan, *The accuracy of quantitative image matching for HRTEM applications*, Materials Characterization, **54**[3]:194-205, 2005.

75 G. Möbus, M. Rühle, *Structure determination of metal-ceramic interfaces by numerical contrast evaluation of HRTEM micrographs*, Ultramicroscopy, **56**[1–3]:54-70, 1994.

76 R. Edwin García; John Blendell (2012), *Equilibrium Wulff Shape Generator*, https://nanohub.org/resources/wulffman. (DOI: 10.4231/D3VM42W8Z).

77 V. Ghetta, D. Chatain, *Morphologies Adopted by Al_2O_3 Single-Crystal Surfaces in Contact with Cu Droplets*, Journal of the American Ceramic Society, **85**[4]:961-964, 2002.

78 R. Akiva, A. Berner, W. D. Kaplan, *The Solubility Limit of CaO in α-Alumina at 1600°C*, Journal of the American Ceramic Society, 2013.

79 V. K. Kumikov, K. B. Khokonov, *On the measurement of surface free energy and surface tension of solid metals*, Journal of Applied Physics, **54**[3]:1346-1350, 1983.

80 P. Wynblatt, D. Chatain, *Surface Segregation Anisotropy and the Equilibrium Shape of Alloy Crystals*, Reviews on Advanced Materials Science, **21**[44-56, 2009.

81 M. McLean, H. Mykura, *The temperature dependence of the surface energy anisotropy of platinum*, Surface Science, **5**[4]:466-481, 1966.

82 T. Wang, C. Lee, L. D. Schmidt, *Shape and orientation of supported Pt particles*, Surface Science, **163**[1]:181-197, 1985.

83 W. H. Lee, K. R. Vanloon, V. Petrova, J. B. Woodhouse, C. M. Loxton, R. I. Masel, *The equilibrium shape and surface energy anisotropy of clean platinum*, Journal of Catalysis, **126**[2]:658-670, 1990.

84 A. S. Ramachandran, S. L. Anderson, A. K. Datye, *The effect of adsorbate and pretreatment on the shape and reactivity of silica-supported platinum particles*, Ultramicroscopy, **51**[1–4]:282-297, 1993.

85 G. Rupprechter, H.-J. Freund, *Adsorbate-induced restructuring and pressure-dependent adsorption on metal nanoparticles studied by electron microscopy and sum frequency generation spectroscopy*, Topics in Catalysis, **14**[1-4]:3-14, 2000.

86 M. Cabié, S. Giorgio, C. R. Henry, M. R. Axet, K. Philippot, B. Chaudret, *Direct Observation of the Reversible Changes of the Morphology of Pt Nanoparticles under Gas Environment*, The Journal of Physical Chemistry C, **114**[5]:2160-2163, 2010.

87 L. Vitos, A. V. Ruban, H. L. Skriver, J. Kollár, *The surface energy of metals*, Surface Science, **411**[1–2]:186-202, 1998.

88 H. L. Skriver, N. M. Rosengaard, *Surface energy and work function of elemental metals*, Physical Review B, **46**[11]:7157-7168, 1992.

89 T. Ning, Q. Yu, Y. Ye, *Multilayer relaxation at the surface of fcc metals: Cu, Ag, Au, Ni, Pd, Pt, Al*, Surface Science, **206**[1–2]:L857-L863, 1988.

90 S. M. Foiles, M. I. Baskes, M. S. Daw, *Embedded-atom-method functions for the fcc metals Cu, Ag, Au, Ni, Pd, Pt, and their alloys*, Physical Review B, **33**[12]:7983-7991, 1986.

91 A. M. Rodríguez, G. Bozzolo, J. Ferrante, *Multilayer relaxation and surface energies of fcc and bcc metals using equivalent crystal theory*, Surface Science, **289**[1–2]:100-126, 1993.

92 M. R. Castell, *Scanning tunneling microscopy of reconstructions on the $SrTiO_3$(001) surface*, Surface Science, **505**[0]:1-13, 2002.

93 Q. D. Jiang, J. Zegenhagen, *c(6×2) and c(4×2) reconstruction of $SrTiO_3$(001)*, Surface Science, **425**[2–3]:343-354, 1999.

94 T. Nishimura, A. Ikeda, H. Namba, T. Morishita, Y. Kido, *Structure change of TiO_2-terminated $SrTiO_3$(001) surfaces by annealing in O_2 atmosphere and ultrahigh vacuum*, Surface Science, **421**[3]:273-278, 1999.

95 M. S. Martín González, M. H. Aguirre, E. Morán, M. Á. Alario-Franco, V. Perez-Dieste, J. Avila, M. C. Asensio, *In situ reduction of (100) $SrTiO_3$*, Solid State Sciences, **2**[5]:519-524, 2000.

אפיון מבנה ותרמודינאמיקה של משטחי ביניים בין Pt ו-$SrTiO_3$

אנה אלטברג

אפיון מבנה ותרמודינאמיקה של משטחי ביניים בין Pt ו-$SrTiO_3$

חיבור על מחקר

לשם מילוי חלקי של הדרישות לקבלת התואר מגיסטר

למדעים בהנדסת חומרים

אנה אלטברג

הוגש לסנט הטכניון – מכון טכנולוגי לישראל

כסלו תשע"ד **חיפה** **נובמבר 2013**

תודות

ברצוני להודות לפרופסור ויין קפלן על הנחייה והעזרה הרבה שקיבלתי ממנו במשך תקופת המחקר.

כמו כן, אני רוצה להודות לחברי בטכניון, ובמיוחד לעמיתיי מקבוצת המחקר קרמיקה ומשטחי הביניים על התמיכה וידידות.

תודה מיוחדת לדר. ירון קאופמן, דר אלכס ברנר ומיכאל קלינה על עזרתם הרבה.

אני מודה לטכניון וקרן על שם ג'ואן וג'יקוב אירווין על התמיכה הכספית הנדיבה בהשתלמותי.

וברצוני להגיד תודה מיוחדת למשפחתי וחבריי, ובמיוחד לבעלי על התמיכה הרבה וסבלנות אינסופית.

תקציר

ננו חלקיקים של מתכות ואוקסידים מהווים מוקד עניין עבור הרבה מתעשיות המודרניות כמו תעשיית המיקרואלקטרוניקה, תעשיית הזרזים, חיישנים, התקני זיכרון ועוד, כל זה הודות לפוטנציאל הרב הטמון בהם. תכונות מיוחדות של ננו חלקיקים נובעות מכך שחלק גדול מהאטומים נמצאים על פני השטח או בסמיכות לו, וכתוצאה מכך, הרבה פעמים החומרים מפגינים תכונות חדשות (תכונות אלקטרוניות, אופטיות, מגנטיות, קטליטיות ומכאניות), שלא מאפיינות אותם כשמדובר בסקאלות יותר גדולות.

הרבה מהתכונות של ננו-חלקיקים נקבעים ע״י מצבם התרמודינאמי כגון צורת שיווי משקל שלהם, אנרגיית משטח הביניים בין החלקיקים והמצע שעל ידיו הם נתמכים, רקונסטרקציה ו/או רלקסציה במשטחי ביניים וספיחה של צורונים אחרים על פני השטח. חלק גדול מפרמטרים אלה תלויים באווירה שבה התעצבו החלקיקים ובתהליכים שאליהם הם היו נתונים. באופן כללי, בגלל שמדובר בחלקיקים מאוד קטנים, הם אמורים להגיע לשיווי משקל בזמנים יחסית קצרים בטמפרטורות מתונות.

מטרת מחקר זה הייתה להעמיק הבנה בתחום של ננו חלקיקים על ידי הסתכלות עליהם מבחינה תרמודינאמית. המטרה הייתה לקבוע את צורת שיווי משקל של החלקיקים, למדוד את אנרגיית משטח הביניים בין החלקיקים והמצע התומך (הנחוצה בשביל לקבוע את מידת האדהזיה של החלקיקים למצע) ולהסתכל על המבנה האטומי במשטחי ביניים. הרעיון היה לשלב את מיטב השיטות המיקרוסקופיות כמו דיפרקציית קרני X, מיקרוסקופיה אלקטרונית סורקת, מיקרוסקופיה אלקטרונית חודרת ועוד, זאת בנוסף לסימולציות מתקדמות של מבנה אטומי (סימולציות של תמונות של מיקרוסקופ אלקטרוני חודר) יחד עם שימוש בשיטת Winterbottom לחקר אנרגיות פני השטח ומשטחי ביניים, על מנת לקבל תמונה מלאה יותר של מצב תרמודינאמי של הננו-חלקיקים שהגיעו לשיווי משקל על גבי המצע.

המערכת שנבחרה לשמש כמערכת מודל בשביל מחקר זה היא פלטינום על גבי חד גביש של -(100) $SrTiO_3$. לאחרונה יש עניין רב במערכת זו הודות לחוסר התאמה קטן בפרמטר השריג שלהם (פחות מחצי אחוז), מה שנותן תקווה שניתן לקבל פלטינום בעל אותה אוריינטציה כמו המצע (משטח ביניים הטרו-אפיטקסיאלי). מערכת זו היא אטרקטיבית במיוחד עבור תחומים כמו מיקרואלקטרוניקה, זרזים והתקני זיכרון. נכון להיום מספר קבוצות בעולם הצליחו לקבל שכבה הטרו-אפיטקסיאלית של פלטינום על גבי (100) $SrTiO_3$, אך מדובר בשיטות יצור שאינן בשיווי משקל כמו : גידול אפיטקסיאלי, התזה, שיקוע בעזרת לייזר ועוד. העבודות שנעשו על מערכת זו נבדלו זו מזו בתנאי הניסוי כמו גם בתוצאות שלהן. לכן, ניתן להסיק מכאן שהמערכת רגישה לסביבה ותנאי הניסוי להם היא נחשפת.

$SrTiO_3$ הינו חומר ממשפחת פרובסקיט ובעל 2 סיומות אפשריות: SrO ו-TiO_2. מחקרים קודמים הראו של פלטינום יש זיקה כימית שונה ל-2 הסיומות וכנראה קיים קשר חזק יותר עם סיומת של TiO_2. מצעים שנעשה בהם שימוש במחקר זה הינם מצעים תעשייתים, המלוטשים מצד אחד ובעלי זווית הטיה של עד חצי מעלה. זה אומר ש-2 הסיומות של $SrTiO_3$ נמצאות בפני השטח. לכן, לפני שיקוע של הפלטינום, המצע עבר טיפול כימי,המקובל במקרים אלה,על מנת שיהיה בעל סיומת אחידה של TiO_2. לאחר טיפול זה, שכבה דקה בעובי של 50 ננומטר של פלטינום שוקעה על גבי המצע בשיטת האידוי. השכבה ששוקעה הייתה רב גבישית ואחידה. ננו-חלקיקים של פלטינום התקבלו בתהליך שנקרא dewetting. זהו תהליך שבו שכבה דקה,אשר נמצאת במצב מטה-סטאבילי, מתפרקת ומתגבשת לחלקיקים/טיפות. תהליך זה יכול לקרות במצב נוזלי או מוצק, ספונטני או יזום. במחקר זה, תהליך ה – dewetting היה יזום ובמצב מוצק. המצע יחד עם השכבה חוממו ב-1050^oC (טמפרטורה שנמוכה יותר מטמפרטורה ההתכה של 2 החומרים) למשך 10 שעות בנוכחות הגז $Ar/2\%O_2$. בעקבות תהליך זה, שכבת פלטינום שלפני זה הייתה רציפה התפרקה ונוצרו חד גבישים של פלטינום. הסיבה שהחימום נעשה בנוכחות חמצן היא כי בסדרת ניסויים דומים, אך ללא נוכחות חמצן, נוצרה פאזה נוספת, לא רצויה, במשטח ביניים בין חלקיק למצע.

מורפולוגיה של המערכת אחרי ה – dewetting נבדקה ע״י מיקרוסקופ אלקטרוני סורק. הבדיקה העלתה שלא כל החלקיקים הגיעו לשיווי משקל, אבל לכל החלקיקים הייתה אותה צורה אופיינית. בנוסף המצע היה מאוד מחוספס והחלקיקים ישבו על גרם מדרגות של המצע. כל זה העלה השערה שבמהלך החימום חלק מהמצע התאדה(למרות שטמפרטורת הניסוי הייתה נמוכה בהרבה מטמפרטורת ההתכה שלו) ופירוק והתגבשות של שכבת הפלטינום התבצע בשלבים. כל שלב כזה הותיר אחריו עוד מדרגה.ניתן היה לראות מדרגות בחלק מהפאות על החלקיקים שטרם הגיעו לשיווי משקל. מדרגות אלה מלמדות שהחלקיקים מגיעים לצורת שיווי משקל במודל TLKהמתאר את אופן גידולם של גבישים.

יחסי אוריינטציה בין מצע לחלקיקים נבדקו בעזרת דיפרקציית קרני X. הציפייה הייתה לקבל משטח ביניים הטרו-אפיטקסיאלי, אך בפועל יחסי אוריינטציה אלה לא התקבלו. הכיווניות המועדפת היחידה שהתקבלה היא של מישורי {111} Pt כמעט מקבילים למישורים של פני השטח (100) $SrTiO_3$ (מישורי {111} Pt הפגינו הטיה של כמה מעלות ביחס לפני השטח). חלקיקי פלטינום לא הפגינו שום אוריינטציה מועדפת בתוך המישור.

בשביל אנליזת צורת שיווי משקל של החלקיקים והמבנה האטומי של משטחי ביניים נעשו דגמים למיקרוסקופ אלקטרוני חודר בעזרת מכשיר FIB. שיטה זו מאפשרת להכין את הדגם בעל אוריינטציה מסוימת ולהסתכל על חתך הפרופיל של החלקיק. צורת שיווי משקל של החלקיק נקבעת בעזרת שילוב של פענוח דיפרקציות אלקטרוניות ביחד עם ניתוח של צורה של החלקיק בשיטת Winterbottom ותוך כדי השוואת התוצאות לסימולציות. התוצאות הראו שצורת שיווי משקל של חלקיק פלטינום שנוצר בנוכחות חמצן כוללת פאות ממשפחות הבאות: {111}, (100),

{110} ו-{113}. יתכן וקיימות פאות נוספות בצורת שיווי משקל, אך הן הינן בעלות אנרגיה גבוהה ולכן קטנות, מה שמקשה יותר על זיהוין.האנרגיות היחסיות של הפאות שהתקבלו הינן: $\gamma(Pt_{113})/\gamma(Pt_{111})=1.065$ ו-$\gamma(Pt_{220})/\gamma(Pt_{111})=1.07$. אנרגיית משטח ביניים בין מצע לחלקיק חושבה להיות: $\gamma(Pt_{111}/STO_{100})=2.08\ J/m^2$. יתכן שגיאה של עד 2% בערכים אלה עקב מגבלות טכניות שונות.

בעזרת מיקרוסקופ אלקטרונים חודר בעל תיקון לאברציה ספרית, התקבלו תמונות של משטח ביניים בעלי רזולוציה אטומית. תמונות אלה אינן יכולות להיות מפורשות בצורה פשוטה כמשמעה, שכן הקונטרסט בתמונות משתנה כפונקציה של עובי של הדגם ופרמטרים של המיקרוסקופ. רק בעזרת ניתוח מעמיק של התמונות ומציאת פרמטרי עבודה של המיקרוסקופ ועובי הדגם (על ידי שימוש בתוכנות סימולציה) ניתן לקבוע מבנה האטומי בתמונה. ניתוח של התמונות מאזור משטח הביניים הראה שקיים שינוי במבנה האטומי במשטח ביניים, כלומר רקונסטרוקציה. אבל, בגלל מגבלות טכניות שונות, טרם ניתן לזהות את הרקונסטרוקציה. כמו כן, אנליזה מקיפה של משטח הביניים בין מצע לחלקיק ופני השטח החופשיים של המצע בסמיכות לחלקיק הראו שלמרות טיפול הכימי שעובר המצע לפני שיקוע של הפלטינום לקבלת סיומת אחידה של TiO_2, הסיומת שהתקבלה אחרי החימום הייתה SrO.

בעצם, בגלל פרמטרי שריג מאוד דומים בין $SrTiO_3$ ופלטינום , הייתה ציפייה לקבל משטח ביניים הטרו-אפיטקסיאלי בשיווי משקל בין ננו-חלקיקים והמצע. בפועל, התקבלו יחסי אוריינטציה יותר מורכבים. אנליזה של משטח ביניים הראתה שמשטח הביניים עבר מספר שינויים בעקבות טיפול ה – dewetting; שינוי בסיומת של המצע כמו גם שינוי בסידור האטומי של המצע. כלומר במשטח ביניים התרחשה רקונסטרוקציה, שזה בעצם complexion והוא זה שמכתיב את יחסי האוריינטציה בין מצע לחלקיק. כלומר, יש כאן עדות שדרגות חופש מיקרוסקופיות השפיעו על דרגות החופש המאקרוסקופיות.